

Geology of the world-class Kiaka polyphase gold deposit, West African Craton, Burkina Faso

Arnaud Fontaine, Aurélien Eglinger, Koumangdiwè Ada, Anne-Sylvie André-Mayer, Laurie Reisberg, Luc Siebenaller, Elodie Le Mignot, Jérôme Ganne, Marc Poujol

▶ **To cite this version:**

Arnaud Fontaine, Aurélien Eglinger, Koumangdiwè Ada, Anne-Sylvie André-Mayer, Laurie Reisberg, et al.. Geology of the world-class Kiaka polyphase gold deposit, West African Craton, Burkina Faso. Journal of African Earth Sciences, 2017, 126, pp.96-122. 10.1016/j.jafrearsci.2016.11.017 . insu-01397784

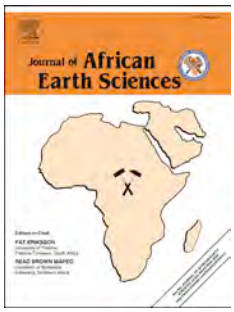
HAL Id: insu-01397784
https://insu.hal.science/insu-01397784

Submitted on 16 Nov 2016

HAL is a multi-disciplinary open access archive for the deposit and dissemination of scientific research documents, whether they are published or not. The documents may come from teaching and research institutions in France or abroad, or from public or private research centers.

L'archive ouverte pluridisciplinaire **HAL**, est destinée au dépôt et à la diffusion de documents scientifiques de niveau recherche, publiés ou non, émanant des établissements d'enseignement et de recherche français ou étrangers, des laboratoires publics ou privés.

Accepted Manuscript



Geology of the world-class Kiaka polyphase gold deposit, West African Craton, Burkina Faso

Arnaud Fontaine, Aurélien Eglinger, Koumangdiwè Ada, Anne-Sylvie André-Mayer, Laurie Reisberg, Luc Siebenaller, Elodie Le Mignot, Jérôme Ganne, Marc Poujol

PII: S1464-343X(16)30374-0

DOI: 10.1016/j.jafrearsci.2016.11.017

Reference: AES 2730

To appear in: *Journal of African Earth Sciences*

Received Date: 12 May 2016

Revised Date: 10 November 2016

Accepted Date: 14 November 2016

Please cite this article as: Fontaine, A., Eglinger, A., Ada, K., André-Mayer, A.-S., Reisberg, L., Siebenaller, L., Le Mignot, E., Ganne, J., Poujol, M., Geology of the world-class Kiaka polyphase gold deposit, West African Craton, Burkina Faso, *Journal of African Earth Sciences* (2016), doi: 10.1016/ j.jafrearsci.2016.11.017.

This is a PDF file of an unedited manuscript that has been accepted for publication. As a service to our customers we are providing this early version of the manuscript. The manuscript will undergo copyediting, typesetting, and review of the resulting proof before it is published in its final form. Please note that during the production process errors may be discovered which could affect the content, and all legal disclaimers that apply to the journal pertain.

ACCEPTED MANUSCRIPT

Geology of the world-class Kiaka polyphase gold deposit, West African Craton, Burkina Faso

Arnaud Fontaine[1, 2]*, Aurélien Eglinger[3,4], Koumangdiwè Ada[5], Anne-Sylvie André-Mayer[1], , Laurie Reisberg[6], Luc Siebenaller[7, 8], Elodie Le Mignot[1, 6], Jérôme Ganne[7], Marc Poujol[9]

[1] GeoRessources, Université de Lorraine-CNRS-CREGU, BP 70239, F-54506, Vandœuvre-lès-Nancy Cedex, France

[2] Institut national de la recherche scientifique, 490 rue de la couronne, G1K 9A9, Quebec City, QC, Canada,

[3] Center for Exploration Targeting, The University of Western Australia, 35 Stirling Highway, Crawley, Perth, Western Australia 6009, Australia

[4] Laboratoire Chrono-environnement, Université de Franche-Comté, UMR CNRS 7249, 16 route de Gray 25030 Besançon, France

[5] B2Gold Corp. Suite 3100, 595 Burrard Street, PO Box 49143, V7X 1J1, Vancouver, British Columbia, Canada

[6] Centre de Recherches Pétrographiques et Géochimiques (CRPG), CNRS-Université de Lorraine, 15 rue Notre-Dame des Pauvres, F-54501 Vandœuvre-lès Nancy, France

[7] IRD, UR 234, GET, Université Toulouse III, 14 Avenue Edouard Belin, 31400, Toulouse, France

[8] ONG-D « Le Soleil dans la Main » asbl, 48, Duerfstrooss, L-9696 Winseler, Luxembourg

[9] Géosciences Rennes, UMR CNRS 6118, OSUR, Université de Rennes 1, 35042, Rennes Cedex, France

*Corresponding author:

Arnaud Fontaine

Centre Eau Terre Environnement

Institut national de la recherche scientifique

490, rue de la couronne, G1K 9A9, Quebec city, CANADA

E-mail: arnaud.fontaine@ete.inrs.ca

Keywords: orogenic gold deposit, Eburnean orogeny, metamorphism, magmatism, Birimian volcano-sedimentary belt, U-Pb and Re-Os geochronology

ACCEPTED MANUSCRIPT

Abstract

The Kiaka gold deposit is a major resource in West Africa, with measured and indicated resources of 124 Mt at 1.09 g/t Au (3.9 Moz) and inferred resources of 27 Mt at 0.83 g/t Au (0.8 Moz). Located within the Manga-Fada N'Gourma greenstone and plutonic belt in south of the Burkina Faso, the deposit is hosted by a metamorphosed volcano-sedimentary sequence of lithic-, quartz-biotite metagreywacke, aluminosilicate-bearing metapelites and garnet-orthopyroxene-bearing schists and volcanic units.

Structural observations indicate four local deformation events: DK_1, DK_2 and DK_3 and DK_4. Respectively, these events are linked to regional D_1 E-W compression, D_2 NW-SE compression and lastly, D_3- and D_4-related reactivations along D_2 shear zones. The S_2 foliation and D_2-related shear zones are developed during lower amphibolite facies metamorphism whereas retrogression occurs during D_{3-4} reactivations along these shear zones at upper greenschist facies conditions. The emplacement of a dioritic intrusion, dated at 2140 ± 7 Ma (Concordia U-Pb age on magmatic zircon), is interpreted to be contemporaneous with sinistral displacement along mineralized, NE-trending D_2 shear zones. The intersection of these shears zones and the Markoye shear zone (dextral-reverse D_1 and sinistral-reverse D_2 reactivations) controlled the final geometry of the host rocks and the ore zones.

Four subparallel elongated ore bodies are mainly hosted within D_2-related shear zones and some are developed in an apparent axial plane of a F_2 isoclinal fold. Detailed petrographic studies have identified two main types of hydrothermal alteration associated with two stages of gold mineralization. The stage (1) corresponds to replacement zones with biotite and clinozoisite during the D_2 event associated with pyrrhotite ± pyrite, chalcopyrite (disseminated gold stage). The stage (2) occurs during reactivations of the D_2-related auriferous shear zones (vein stage) and are characterized by diopside ± actinolite D_3 veins and veinlets and D_4 pervasive muscovite, ± chlorite, ± calcite in quartz-carbonate vein selvages and associated with pyrrhotite + arsenopyrite ± electrum, ± native gold and tellurobismuthite. The latter stage (2) could be divided into two sub-stages based on mineralogy and crosscutting relationship. A weighted average Re-Os pyrrhotite age at 2157 ± 24 Ma (Re-Os age based on 3 replicates) constraints the timing of the disseminated gold stage and represents the first absolute age for gold mineralization in the Manga Fada N'Gourma area. The timing of gold at Kiaka may be also coeval with one of the two lode gold event at ~ca. 2.16-2.15 Ga and occurred concomitant with tectono-thermal activity during Eo-Eburnean orogeny.

The study of the Kiaka gold deposit emphasizes the importance of a multi-scale and multidisciplinary approach (field observations, petrography geothermobarometry and geochronology) to decipher the polyphase character of some Paleoproterozoic gold deposits.

Introduction

Orogenic gold deposits represent a major source for global gold production (Goldfarb et al. 2001, Frimmel, 2008). These ore deposits formed from the Paleoarchean (gold mineralization in the Pilbara craton dated at ca. 3.4-3.3 Ga; Neumayr et al. 1998) to the early Cenozoic (gold-bearing quartz veins in the Southern Alps formed during the last 7 Ma; Craw and Koons 1989). The term "orogenic" is linked to their close association with accretionary and collisional orogens (Groves et al., 1998). Ore in such deposits is (i) epigenetic and hosted by deformed and variably metamorphosed rocks at mid- to shallow crustal levels (Böhlke 1982; Goldfarb et al. 2001, 2005), (ii) spatially associated with major crustal structures (Sibson et al. 1988; Colvine et al. 1988; Kerrich et al. 2000). Some authors have also argued for a spatial and/or temporal association between gold and granitoids of variable composition (Colvine et al. 1988; Champion and Sheraton 1997; Cassidy et al. 2002; Goldfarb et al. 2005; Doublier et al. 2014). The relationship between gold and magmatism is probably due to the the late-orogenic extensional tectonics that also focuses plutonism along auriferous structures. Granites can also provide thermal perturbations, competence contrasts at belt to deposit scale and/or may also contribute some metals and/or ligands that are district specific (Wyman et al., 2016).

Crustal scale processes are invoked for the formation of orogenic gold systems (McCuaig and Hornsky, 2014; Wyman et al., 2016) as they form in a very short time in relation with tectonic triggers, controlling the transfer of fluids within the crust (Sibson et al., 1988; Cox, 2005; Weatherley and Henley, 2013). They are products of aqueous-carbonic fluids released during metamorphic reactions in middle to lower crust. Increases in disequilibrium between fluids and host rock induce destabilization of gold-carrying complexes such as $Au(HS)_2$ and AuHS (Tomkins, 2013). Possible sources of fluids for orogenic gold deposits are: (1) metamorphic rocks and fluids generated with increasing metamorphism and (2) felsic intermediate magmas and associated fluids. The first source is very consistent with geological, geochronological and geochemical data (Goldfarb and Groves, 2015), while the second source remains inconsistent as no universal temporal link has been described to date.

ACCEPTED MANUSCRIPT

The Baoulé-Mossi domain (Abouchami and Boher 1990; Boher et al. 1992; Taylor et al. 1992) hosts abundant gold deposits (Fig. 1) within deformed volcanic and sedimentary rocks that have undergone regional greenschist to locally contact amphibolite facies metamorphism (Béziat et al. 2000, 2008; Castaing et al. 2003; Ganne et al. 2011).

Combined structural and Re-Os and U-Pb geochronology performed respectively on hydrothermal pyrite and arsenopyrite, and hydrothermal accessory minerals such as monazite or rutile (Pigois et al., 2003; Tunks et al., 2004; McFarlane, 2011; White et al., 2014), that have been considered petrographically as gold proxy (Le Mignot 2016a; Le Mignot et al. 2016b; Markwitz et al., 2015) highlight two groups of orogenic gold deposits. An Early-orogenic gold group formed during the Eoeburnean orogeny, i.e., between 2190 and 2125 Ma (Wassa1, Kiaka1) (Perrouty et al. 2015; Le Mignot et al., 2016) while a second late-orogenic gold group hosted by brittle structures, formed during late Eburnean deformation, between 2120 and 2000 Ma (Obuasi, Damang, Nassara, Wassa2, Kalana, Loulo, Poura, etc). These lode gold events seem to be widespread through the West African Craton (See fig. 2 in Markwitz et al., 2016; and references therein, Le Mignot et al. 2016b).

The Kiaka gold deposit is located at 140 km southeast of the capital Ouagadougou. Owned by B2Gold Corp. (Volta Resources formally), the deposit has measured and indicated resources of 124 Mt at 1.09 g/t Au (3.9 Moz) and inferred resources of 27 Mt at 0.93 g/t Au (0.8 Moz; B2Gold Corp., January 2013). In March 2014, B2Gold Corp. submitted a permitting study to the Ministry of Mines in Burkina Faso together with a mining licence application.

This paper will present the geological features of the Kiaka gold deposit, one of the largest undeveloped gold resources in Burkina Faso, which expresses a multistage gold mineralization. The Kiaka gold deposit is hosted by metamorphosed sedimentary rocks, from greenschist to amphibolite facies that are affected by syn- to late-orogenic magmatism. The relative timing of gold mineralization relative to metamorphic and magmatic events is unclear. The geological features of the Kiaka deposit will be described, combining structural, petrographic, mineralogical, thermobarometric and geochronological studies (U-Pb on zircon and Re-Os on pyrrhotite). The timing of the gold mineralization and magmatic events will be replaced within the metamorphic evolution of the considered crustal segment (Ganne et al., 2011). Key geological features will be discussed for exploration implication in the Baoulé-Mossi domain, a juvenile Paleoproterozoic crust that hosts major gold districts.

ACCEPTED MANUSCRIPT

FIGURE 1

Regional geological framework

The West African Craton (WAC) consists of an Archean nucleus (Kénéma Man domain) that is surrounded by 2.25 to 2 Ga Paleoproterozoic greenstone belts of the Baoulé-Mossi domain (Feybesse and Milesi 1994; Feybesse et al. 2006; Fig. 1). The Baoulé-Mossi domain comprises Birimian greenstone belts (volcanic and volcano-sedimentary rocks) intruded by Tonalite-Trondhjemite-Granodiorite (TTG) suites and granitoids (Leube et al. 1990; Doumbia et al. 1998; Gasquet et al. 2003; Dioh et al. 2005, Davis et al. 2015). The volcanic rocks vary in composition from basalt with tholeiitic and/or calc-alkaline affinities to rhyolite. Basalts are interpreted as oceanic crust (Leube et al. 1990; Ama Salah et al. 1996; Béziat et al. 2000; Baratoux et al. 2011) or oceanic plateau basalts (Abouchami and Boher 1990; Boher et al. 1992; Vidal et al. 1996; Doumbia et al. 1998; Lompo 2009). Rhyolites are associated with juvenile calc-alkaline volcanic island arc-style rocks (Baratoux et al. 2011 and references therein). Tholeiitic volcanic rocks are dated at 2.17 Ga (Taylor et al. 1992: Simeon et al. 1992; Hirdes and Davis 1998) and the TTG intrusions vary in age from ca. 2.25 to 2.10 Ga, representing a major period of crustal growth (Hirdes et al. 1996; Doumbia et al. 1998; Lüdtke et al. 1998, 1999; Oberthür et al. 1998; Castaing et al. 2003; Gasquet et al. 2003; Feybesse et al. 2006; Agyei Duodu et al. 2009; Siegfried et al. 2009; Thomas et al. 2009; Eglinger et al. 2015). TTG magmatism was accompanied by the deposition of the Birimian volcanic and sedimentary rocks (Baratoux et al., 2011). Until ca. 2.07 Ga, potassic and peraluminous granites are contemporaneous with late transcurrent shearing (Hirdes et al. 1992; Davis et al, 1994; Doumbia et al. 1998; Egal et al. 2002; Castaing et al. 2003; Vegas et al. 2007). Intrusive rocks have been divided into three groups based on petrography, geochemistry and radiometric ages (Baratoux et al. 2011) and on airborne magnetic and radiometric signatures (Metelka et al. 2011). The first magmatic episode (ME1) is characterized by calc-alkaline biotite and amphibole-bearing TTG suites dated from ca. 2.16 to 2.12 Ga. The second episode (ME2) is represented by calc-alkaline K-feldspar and biotite-bearing granodiorite-granite intrusions dated from ca. 2.12 to 2.09 Ga. The third episode (ME3) is dominated by potassic feldspar-bearing granites that are associated with late orogenic stages at ca. 2.11 and 2.07 Ga. At a regional scale, multiple tectonic phases related to Eo- or -Eburnean orogeny are recognized (Baratoux et al. 2011; Perrouty et al., 2012; Block et al., 2015). The D_1 deformation is defined as E-W to WNW compression illustrated by isoclinal folds and local shear zones. The D_2 event is

ACCEPTED MANUSCRIPT

defined by regional, sinistral NS trending or dextral E-NE-trending anastomosing shear zones (Baratoux et al., 2011). The late-D_2 to D_3 phase is illustrated by the development of N- to NE-trending transcurrent shearing (D_2-related shear zones). Following the main period of tectonic amalgamation of the various volcano-sedimentary belts between ca. 2.20 and 2.15 Ga (Feybesse et al. 2006), the Baoulé-Mossi Paleoproterozoic crust was deformed during the Eburnean orogeny from ca. 2.15 to 2.00 Ga (Bonhomme 1962; Feybesse et al., 2006; Baratoux et al., 2011). The latter is divided in two phases: the ca. 2.250-2.150 Tangean event (Tshibubudze et al. 2009; Hein, 2010) or Eoeburnean (Perrouty et al. 2012), and the ca. 2.15 to 1.98 Ga Eburnean II phase (Baratoux et al. 2011).

The Birimian formations are unconformably overlain by Tarkwaian, syn- to late-orogenic sedimentary sequences (conglomerate and quartzite) with a maximum age varying between ca. 2.17 and 2.12 Ga (Davis et al. 1994; Bossière et al. 1996; Perrouty et al. 2012, Davis et al. 2015).

The southeastern part of Burkina Faso (the Manga-Fada N'Gourma area) is characterized by a volcano-sedimentary sequence and plutonic rocks, which are bounded or crosscut by high-strain shear zones (i.e. Fada N'Gourma belt described by Naba et al. 2003 and Ganne et al. 2011, Fig. 2). The area is cut by the Markoye shear zone (MSZ), a major N-S oriented crustal-scale structure of 450 km formed during D_1 and reactivated during D_2 (Tshibubudze et al., 2009 and Tshibubudze and Hein, 2013; Fig. 2) and that crosscuts several distinct volcano-sedimentary belts. This structure has recorded multiple reactivation events as distinguished by Tshibubudze et al. (2009) in its northern part (North Burkina Faso). Several orogenic gold deposits are associated with the MSZ within the Aribinda-Essakhane (Essakhane; Tshibubudze et al., 2015), Bouroum-Yalago (Gangaol, Taparko, Béziat et al., 2008) and Manga-Fada-N'Gourma (this study) greenstone belt (Fig. 1). The Kiaka gold deposit is located at the intersection between the MSZ and several smaller D_2 NE-SW trending shear zones (Fig. 2). These shear zones are roughly parallel to a series of metamorphosed volcano-sedimentary belts bounded by plutonic belts (Hottin and Ouédraogo 1976, 1992; Castaing et al. 2003; Naba et al. 2003; Vegas et al. 2007). The Manga-Fada N'Gourma greenstone belt predominantly consists of metamorphosed pelites, greywackes and volcanic rocks, including basaltic to andesitic coherent lava flows and volcaniclastic rocks (Hottin and Ouédraogo 1976; Castaing et al. 2003).

FIGURE 2

Materials and methods

Structural data

Structural analysis was done on oriented drill core (Fig. 3) and on rare outcrops of deformed quartz-biotite metagreywacke and aluminosilicate-bearing metapelites (Figs. 3 and 8). DK_X will be used to describe the different deformation events described on drill cores and outcrops from the Kiaka deposit and SK_x, LK_x and FK_x for foliation, lineation and folding, respectively.

Geochemical analyses of whole rocks and minerals

Major and trace elements (Table 1) were determined by ICP-AES and ICP-MS at the Service d'Analyse des Roches et des Minéraux**,** Nancy (SARM, CRPG-CNRS, France) on four whole-rock samples from the volcano-sedimentary (KDH291-56.2, KDH348-44.5-54.8, KDH75-64.9) and magmatic units (KDH337-44.1). Sample preparation, analytical conditions, uncertainty and limits of detection are detailed in Carignan et al. (2001) and in http://helium.crpg.cnrs-nancy.fr/SARM/pages/roches.html. For all elements, error are < 0,01% and uncertainty are < 5%. Geochemical reference materials are Basalt BR, Diorite DR-N, Serpentinite UB-N, Anorthosite AN-G and Granite GH (Carignan et al., 2001). Data are presented in Table 1.

Microprobe analyses of minerals

SEM (Hitachi S-4800 and JEOL J7600F) and microprobe analyses (Table, 2, 3, 4 and 5) by electron microprobe CAMECA SX100 were performed at GeoRessources (Nancy, France). For analyses and quantitative mapping, an accelerating voltage of 20 kV, beam current of 12 nA and peak counting time 10 to 20 s were used. Whole rock lithogeochemical data and in situ silicates and sulfides data are presented in Tables 1 to 7. For the Table 5, mineral chemical analyses within rocks were carried out at the GET at Université Toulouse III, France, using a Cameca SXFIVE electron microprobe analyser. Operating conditions were 15 kV, 20 nA, 1–5 µm beam size and counting time of 10 s/per element. CO_2 was neglected because no carbonates were observed in the meta-sedimentary rocks analysed.

ACCEPTED MANUSCRIPT

Geothermobarometry

Phase diagram has been used to constraint P-T conditions of the calc-silicate schists which have recorded the conditions at the peak of metamorphism. These diagrams have been computed using Perple_X 6.6.8 (Connolly, 2005, 2009) and the updated 2002 version of the internally consistent thermodynamic database of Holland and Powell (1998). For solid solutions, we used the internally consistent thermodynamic dataset termed solution_model.dat (December 10, 2014; available at www.perplex.ethz.ch/).

ICP-MS and N-TIMS Re-Os dating

Re-Os dating on sulfides (Stein et al. 2000; Brenan et al. 2000; Reisberg and Miesel 2002, Selby et al., 2002; Selby and Creaser 2004; Mathur et al. 2005; Cardon et al. 2008; Lü et al. 2011, André-Mayer et al. 2014) is a useful tool for dating ore deposits. Sulfide powders, added with an appropriate quantity of a mixed ^{185}Re-^{190}Os spike and 0.1 mL of hydrogen peroxide, were dissolved in reverse aquia regia (2 mL HCl, 5 mL HNO_3) using a high pressure asher (HPA-S Anton Paar). Sample digestions were carried out for 3 hours at 300°C, under 130 bars of confining pressure. After sample digestion, Os was separated by liquid-liquid extraction into liquid bromine (Birck et al. 1997); Re was extracted from the residual solution by anion exchange using chromatographic columns (AG1 X8 resin). Os was then purified by micro-distillation (Birck et al., 1997). Re measurements were made using an inductively coupled plasma mass spectrometer (ICP-MS) (Neptune, in CRPG, Nancy). Instrumental mass fractionation was regularly monitored during measurements using a 0.3 ppb Re standard. Os was analyzed by negative thermal ionization mass spectrometry (N-TIMS; Creaser et al. 1991; Völkening et al. 1991) using a Finnigan MAT 262 instrument, CRPG). Instrumental mass fractionation was corrected iteratively off-line by assuming that the true ^{192}Os/^{188}Os ratio of the sample lay on a mixing line between the natural value (3.08271) (Nier, 1937) and the measured spike value (5.00736) (Le Mignot, 2014). Corrections for isobaric interferences of isotopically heavy oxides were done using the oxygen isotopic composition of Nier, (1950) (^{17}O/^{16}O = 0.0003708 and ^{18}O/^{16}O = 0.002045).

Total Os blanks linked to chemical preparation and mass spectrometric measurements range from 0.04 to 0.16 pg (3 analyses). The ^{187}Os contents of these blanks are comprised between 0.01 and 0.08 pg and are considered as insignificant when compared to the quantities of radiogenic Os in the samples. Re blank values are higher,

ranging between 3.9 and 8.3 pg. They nevertheless always represent less than 0.4% of the quantities of the Re present in the samples. Uncertainties related to the blank characterization are included in the total uncertainties. During the period of analysis, the $^{187}Os/^{188}Os$ ratio of our in-house standard was 0.1739 ± 0.0005 (2σ, n=52), which agrees with the value obtained for this standard over the past 8 years (0.1737 ± 0.0008, n=315). Eight replicates of the Henderson molybdenite standard yielded an average age of 27.75 ± 0.15 Ma (2σ-m; n=8), slightly older than the recommended value (27.656 ± 0.022) of Markey et al. (2007).

LA-ICP-MS U-Pb zircon dating

Normal transmitted and reflected light microscopy, as well as cathodoluminescence imaging were used to determine the internal structures of zircon prior to analysis. Analyses by Laser Ablation Inductively Coupled Plasma Mass Spectrometry (LA-ICP-MS) were performed in the Geosciences Rennes laboratory, using a quadripole ICP-MS Agilent 7700x coupled with a 193 nm Excimer laser system ESI (NWR193UC). More details on the analytical procedure can be found in Ballouard et al. (2015). Single analyses consisted of ~20 s of background integration with the laser off, followed by ~60-s integration with the laser firing and then a ~10-s delay for wash out. Zircon grains were ablated using a laser repetition rate of 4 Hz, laser energy of 8J/cm^2 and a beam diameter of 30 μm (carrier gas is He (0.75 l/min), combined with Ar (0.8ml/mn) and N2 (3 ml/mn) using in-house smoothing device). Raw data were corrected for Pb/U and Pb/Th laser-induced elemental fractionation and for instrumental mass discrimination by standard bracketing with repeated measurements of the zircon standard GJ-1 (Jackson et al. 2004). Together with the samples, the zircon standard 91500 (ca 1065 Ma; Wiedenbeck et al. 1995) was measured as an unknown to monitor the precision and accuracy of the analyses and yield a concordia age of 1068 ± 8 Ma (MSWD=1.3; N=4). Data were reduced using GLITTER (Van Achterbergh et al., 2001). Analytical uncertainties are listed at 1σ (Table 8) and age determinations were processed using Isoplot/Ex (Ludwig 2000). Reported data are not corrected for common Pb, however, only pristine zircon domains devoid of inclusions were targeted for U-Pb geochronology.

Local geology and deposit geometry

ACCEPTED MANUSCRIPT

Local geology

The geology of the Kiaka property is characterized by the structurally imbricated metamorphosed mafic rocks, conglomerate, quartz-biotite or lithic metagreywacke, aluminosilicate-bearing metapelites, garnet-orthopyroxene-bearing schist, and quartz-muscovite schist (Fig. 3). Garnet-orthopyroxene-bearing schists are located in the southern part of the deposit, while the lithic greywackes are located in the northern part. These units are usually 200-400m wide, elongated slices striking N035, commonly subparallel to D_2-related shear zones. All units dip to the northwest at 80 to 85°. Thickness of the lithic greywacke varies from 50 to 100 meters. The garnet-orthopyroxene-bearing schist is mainly located in the footwall of the D_2-related shear zone (Fig. 4). A diorite plug (5 to 30 m thick) is located in the north and is structurally controlled by D_2-related shear zones.

FIGURE 3

FIGURE 4

The host rocks at the Kiaka deposit are predominantly metasedimentary (Fig. 5a, b and c) and metavolcanic rocks (Fig. 5e). These include quartz-muscovite schists (Fig 5a) and garnet-orthopyroxene-bearing schist and a dioritic plug (Fig. 5d) intrudes the quartz-biotite and quartz-muscovite schist in the north part of the ore body (Fig. 4a). This contains clasts of amphibolite schists.

Metasedimentary rocks

Aluminosilicate-bearing metapelites (KDH348 – 44.5; Fig. 5c) are located in the south footwall of a DK_2-related shear zone that hosts the main mineralized envelope (Fig. 3). Samples are characterized by a granoblastic to nematoblastic texture (metamorphic texture in which prismatic minerals such as sillimanite or amphiboles are oriented to produce a linear fabric) underscored by a shape-preferred orientation of fibrolite (15-25%) and prismatic sillimanite (5-10%), the latter defining the LK_2 mineral lineation (Fig. 8b). Fine grains of quartz (50-75%) dynamically recrystallized, characterizing a foliation parallel to the sillimanite orientation, are dominant in the matrix. Some rounded kyanite poikiloblasts are also present, wrapped into the SK_2 schistosity. Kyanite crystals replace muscovite (Ms_1; Fig. 6b). Some euhedral biotite crystals are present and locally chloritized. Fine

ACCEPTED MANUSCRIPT

296 euhedral grains (20 to 50 μm) of tourmaline (Tur_1) are also observed in the recrystallized quartz-rich matrix.
297 Lithic greywacke is characterized by feldspar or quartz porphyroclasts (100μm to 0.1mm; 5-75%), biotite (10-
298 25%), chlorite, and rare pyrrhotite.
299
300 *Garnet-orthopyroxene-bearing schist*
301 This schist unit (KDH300-470; Fig. 6c) comprises garnet (15-20%), orthopyroxene (10-15%), amphibole (50-
302 55%), biotite (4-5%), plagioclase (10-15%; An21), and chlorite (5-10%). Biotite and amphibole define a
303 nematoblastic texture. Poikiloblastic garnets (X_{Alm}:0.72) often contain quartz, biotite, amphibole and sulfide
304 inclusions (<50 μm). Orthopyroxene grains (Ferrosilite) are found in equigranular domains in association with
305 amphibole (ferro-hornblende), quartz and phlogopite (Bt_1). Chlorite (Chl_1) is associated with amphibole and
306 biotite (Bt_1) crystals.
307
308 *Diorite*
309 Samples KDH337-44.1 and -69.6 (Fig. 6d) are from the 6100 section, 300 m northeast of the 5800 cross-section
310 (Fig. 4a). Located in the north part of the deposit area, no clear relationships with the stage 1 was observed but
311 sericite, calcite and clinozoisite, pyrrhotite and chalcopyrite are locally present in the intrusion as alteration
312 assemblage related to strained domains. The assemblage is made up of plagioclase (25-30%; An_{27}), amphibole
313 (25-30%), chlorite, biotite (20-25%), and quartz (15-20%), with minor amounts of sulfide (1-2 % of pyrrhotite
314 sometimes associated with rare chalcopyrite) and zircon. Amphibole porphyroblasts (200-500μm) are rimmed by
315 biotite forming corona textures (Fig. 6d). Amphiboles have Mg-hornblende to actinolite compositions with XMg
316 ranging from 0.55 to 0.95 and Ca (apfu) ranging from 1.66 to 2.00 (Table 5).
317
318 **FIGURE 5**
319 **FIGURE 6**
320
321
322 *Geometry of the deposit*
323
324 Four mineralized envelopes at the Kiaka deposit are defined based on drill core data (Fig. 3). Each subparallel
325 envelope is hosted elongated ore bodies mostly hosted by the quartz-biotite metagreywacke underlying the lithic

ACCEPTED MANUSCRIPT

metagreywackes (Figs. 3 and 4b). Lithological contacts are mineralized in 6100 and 5400 sections. In section 5800, the main ore zone is developed in an axial plane of a FK_2 isoclinal fold illustrated by the geometry of the lithic greywacke and also at the contact with D_2 related shear zones that probably juxtaposed this unit with the garnet-orthopyroxene-bearing schist.

Geochemistry

Quartz-muscovite schists (KDH75-64.9) and aluminosilicate-bearing metapelites (KDH348-44.5) have high SiO_2 (78.01 wt.% and 71.66 wt.%) and Al_2O_3 (13.55 wt.% and 15.14 wt.%). Major element analyses of the meta-igneous sample KDH337 show intermediate SiO_2 (57.32 wt.%) and high Al_2O_3 (16.59 wt.%) and CaO (6.57 wt.%) concentrations combined with a total alkali ($Na_2O + K_2O$ = 5.72 wt.%) content and a K_2O/ Na_2O ratio of 0.53 indicating an affinity with the sodic series (Table 1). On the SiO_2 vs. $Na_2O + K_2O$ binary diagram of Cox et al. (1979), this intrusion plots in the field of diorite (Fig. 7a). The Kiaka diorite has high Sr and Ba concentrations, of 748 and 665 ppm, respectively (Table 1). This rock is characterized by strong depletions in Nb, Ta and Ti and a positive Sr anomaly and displays no Eu anomaly, as shown by the primitive mantle-normalized spidergram (Fig. 7b). The Sr/Y ratio is high (~47) compared to the Tenkodogo granitoid (~27; Naba et al., 2003; See Table 1 for details), located 50 km east of the Kiaka gold deposit. The rare earth elements (REE) are fractionated and characterized by low HREE abundances (Yb = 1.48 ppm) and a high $(La/Yb)_N$ ratio (~13; N indicates chondrite normalization after Sun and McDonough, 1995). However, fractionation among the HREE is moderate, as is indicated by the Y/Yb ratio of ~11 and the flat HREE patterns (Fig. 7c). Diorites from the Morila Au deposit (McFarlane et al., 2011), granitoids from Tenkodogo (samples T15 and DD17; Naba et al., 2003) and Fada'N'Gourma area (sample FC97; Vegas et al, 2007) express similar major and trace elements composition.

TABLE 1

FIGURE 7

Structural data

ACCEPTED MANUSCRIPT

DK_1 event: Early penetrative foliation

The first event DK_1 is evidenced by the presence of relic FK_1 folds (Fig. 8a) evidenced by a wide range of fold axis orientations with a moderate plunge (45° to 60°) that diverged from the isoclinal folds with axial planes parallel to the SK_2 cleavage (Fig. 8d). The aluminosilicate-bearing metapelites are affected by such FK_1 folds as illustrated by FK_1/FK_2 interference patterns (Fig 8e) whereas mafic rocks are unaffected by such early deformation (Fig. 8c).

DK_2 event: Metamorphic foliation, shear-related folds and late-DK_2 shear zones

Stretching and mineral lineations LK_2 (Fig. 8b) oriented N352 to N070 with moderate plunges from 52° to 64° are associated with the axial planar SK_2 cleavage/foliation. Prismatic sillimanite commonly defines this mineral lineation. Moderate plunge of ore shoots illustrates effects of oblique shearing along the D_2-related shear zones and/or effects of shallow plunging of the FK_2 fold axis on ore distribution (Fig. 4d). Shear-related asymmetric folds (Fig. 8d) and shear zones oriented 050NE, plunge steeply to the North (Fig. 4b). Sigma-type porphyroclasts and C-S shear bands indicate a sinistral movement (Fig. 8d). Section view illustrates the reverse component of this structural event. These shear zones are spatially associated with the ore zones hosted by the volcano-sedimentary units of the Manga-Fada-N'Gourma area. Ore shoots are roughly collinear with the LK_2 lineation (Figs. 4d) but sometimes appear as following stratigraphic folded contacts or DK_2-related shear zones (Fig. 4b). FK_2 folds limbs are totally transposed in the SK_2 regional foliation and related shear bands. Late-D_2 ME_{2+3} plutons (Ouargaye and Kaouré) are affected by regional D_2-shear zone reactivations (Fig. 2). The diorite intrusion (dated in this study) located in the NE of the deposit are locally affected by shearing, illustrated by the alignment of biotite sheets and actinolite grains.

DK_{3-4} events: Late fracture-controlled veining associated with reactivation along DK_2 shear zones

Based on their orientations and crosscutting relationships (Fig. 11c and e), a distinction is made between DK_3 (N010°) and DK_4 (N100°) faults. DK_4 quartz veins with slivers of metamorphosed and hydrothermally altered metagreywackes, quartz-carbonate-phlogopite or quartz-carbonate extensional veins form a fractured-controlled stockwork locally reworked and reoriented along the SK_2 fabric, preferentially developed at the contact between

ACCEPTED MANUSCRIPT

the metasedimentary sequence and metamorphosed mafic rocks (See Hydrothermal alteration for details). Orientations and dips of DK_{3-4} veins have NE to SW-trending a wide range of dips (15 to 85°) with NE to SW-trending orientations.

FIGURE 8

FIGURE 9

Metamorphism

We investigated the metamorphic history using a combination of conventional geothermobarometry (chlorite, amphibole and arsenopyrite) and metamorphic modelling.

Conventional geothermobarometry

Chlorite temperatures (Table 2) were calculated using the thermodynamic modeling program of Lanari et al. (2014). Chlorite inclusions (Chl_1; Fig. 11e) in tourmaline porphyroblasts from the metabasic sample KDH29-56.2 yielded the lowest temperatures ranging from 269 to 306 °C, corresponding to a mean temperature of 285 ± 50°C (n=4; Table 2). A 2nd generation of chlorite is associated destabilization of biotite porphyroblasts within metabasic rock. This local chloritization stage (Chl_2; Fig. 11) observed in the matrix occurred at temperatures ranging from 371 to 413 °C, corresponding to a mean temperature of 383 ± 50°C (n=7; Table 2).

TABLE 2

Major element compositions of calcic-amphibole from the diorites collected in drillhole KDH337 were analyzed in order to estimate pressure of emplacement (Table 3). From the cores of porphyroblasts, amphiboles associated with biotite (Fig. 10f) are mainly actinolite, but Mg-hornblende is also present (Table 3). We interpret the latter as relicts of magmatic amphibole that was formed during prograde metamorphism and preserved from retrogression and potential coeval hydrothermal alteration. Four different geobarometers (Hammarstrom and Zen, 1986; Hollister et al., 1987; Johnson and Rutherford, 1989 and Schmidt, 1992) were applied to each of the three Mg-hornblende crystals tested. Pressure estimates (Table 3) ranged from 0.92 to 5.65 kbars indicating variable degrees of re-equilibration during retrogression or hydrothermal circulation.

TABLE 3

Metamorphic modeling

A pseudosection approach appears appropriate for assessing changing mineral paragenesis in rock types of homogeneous composition. Our pelitic samples (KDH300-470), collected in the interference zones of the Kiaka area, with a variable D_2 imprint, are characterized by a homogeneous distribution of zoned minerals, such as garnet and orthopyroxene that are unlikely to have modified the bulk rock composition during their growth. The P-T pseudosection were calculated for the Na_2O–CaO–K_2O–FeO–MgO–MnO–Al_2O_3–TiO_2–SiO_2–H_2O system, using bulk rock compositions obtained by XRF analysis and for subsolidus H_2O saturations conditions. The observed mineral assemblage, i.e. garnet-biotite-chlorite-plagioclase-orthopyroxene and orthoamphibole with the presence of ilmenite, ± K-felspar and ± quartz is bivariant and stable over a narrow *P–T* range at 7.5 – 4 kbar and 550 - 400 °C. Perple_X modeling using the compositions of biotite observed as inclusions within the rim of garnets (Table 4) allows the refinement of the inferred peak of metamorphism at P=7.5 kbar and T=550 °C. At this calculated peak, mineral phases are orthopyroxene (6.00 vol%), biotite (3.10 vol%), chlorite (6.71 vol%), plagioclase (65.32 vol%), K-feldspar (6.01 vol%), garnet (2.67 vol%), ilmenite (0.84 vol%), quartz (0.09 vol%) and orthoamphibole (9.25 vol%). These mineral proportions are in good agreement with thin section observation (Fig. 6c). Conditions are regarded as coeval with the DK_2 deformation and diorite emplacement. The Kiaka sedimentary host rocks underwent the M2a prograde near-isobaric heating at 450-650 and 6-8kbar described by Ganne et al., 2014 in metasediments located in high-T aureoles of granitoids plutons recorded.

TABLE 4

Mineralization

Two stages of gold mineralization are identified based on crosscutting relationships, hydrothermal assemblages and ore mineralogy: an early sulfide-rich disseminated stage 1 and a sulfide-poor stage 2. Stage 1 represents at least 80% of the volume of the ore bodies and is located in the quartz-biotite and lithic metagreywackes extending 10 to 150 m from DK_2 high-strain zones. Stage 2 is associated with strongly altered stratigraphic

ACCEPTED MANUSCRIPT

446 contact affected by D_2-related shear zones. Temporal relationships between host rocks, gangue, and ore minerals
447 are summarized in Figure 10. Figures 11 and 12, respectively, illustrate mineralization styles, ore mineralogy,
448 and textures.

449 **FIGURE 10**

450 *Ore styles and textures*

451

452 A wide range of mineralization styles is present at Kiaka including i) a stockwerk of semi-massive pyrrhotite,
453 pyrite and chalcopyrite in association with replacement zones of biotite-clinozoisite (70-80% of ore), ii)
454 hydrothermal breccia composed of hydrothermally altered fragments of pelites, the quartz-rich matrix locally
455 containing diopside and actinolite (10-15% of ore; Fig. 11b), and iii) a network of quartz carbonate veinlets
456 associated with a pervasive alteration assemblage composed of clinozoisite and carbonate (5-10%) and iv)
457 quartz-carbonate-phlogopite veins (rare DK_4). The latter three styles commonly overprint the sulfide dominant
458 ore stage (Fig. 11b, c, d and e).

459

ACCEPTED MANUSCRIPT

ACCEPTED MANUSCRIPT

FIGURE 11

Ore mineralogy

Pyrrhotite (50 µm to 1 mm) accounts for 60-80% of ore phases characterizing the mineralization in stage 1. Pyrrhotite is commonly associated with 10 to 20% of pyrite (200-300 µm), 5 to 10% of chalcopyrite (20-50 µm), 5-10% of pyrite (50 to 200 µm), 5-10% of arsenopyrite (100 to 500 µm) and rare lollïngite inclusions within pyrrhotite or arsenopyrite (<50 µm). Pyrite forms overgrowths or composite aggregates with pyrrhotite and chalcopyrite. Pyrrhotite grains are commonly inclusion-rich (chalcopyrite, quartz and hematite) and fracture-filling chalcopyrite. These sulfides comprise recrystallized aggregates transposed within the SK_2 foliation (Fig. 12a) and locally affected by shearing along DK_2 shear bands (Fig. 11a and Fig. 13a). These characterize the large mineralized envelope of high-grade ore. Some sulfide phases are locally remobilized within necks of elongated microlithons of quartz-rich matrix (Fig 12a). Arsenopyrite is is partially to totally replace by pyrrhotite aggregates (Fig. 12c). Inclusions of lollïngite within pyrrhotite crystals are present in strongly sericitized greywacke (Fig 12c).

The stage 2 contains less abundant sulfides (< 2-3 %) but Bi-Te-rich phases (5-10 µm), electrum (10 to 20 µm), and native gold (2 to 20 µm) are associated with chalcopyrite, pyrrhotite and arsenopyrite (Fig. 12d, e and f). Electrum is found in i) fractures within pyrrhotite, arsenopyrite (Fig. 12e), chalcopyrite and clinozoisite, ii) in chlorite sheets (Fig 12f). Finally, fractures in arsenopyrite associated with electrum in fractures (Fig. 12e).

FIGURE 12

Co content of arsenopyrite (Table 5 and Fig, 12e) are highly variable between arsenopyrite from sericitized greywacke ranging from 0.04 to 0.13 wt.% (mean of 0.08 wt.% Co; n=6) or associated with Chl_2 in chloritized greywacke ranging from 4.52 to 5.41 wt.% (mean of 4.96 wt.% Co; n=2). Arsenic content of arsenopyrites (Table 5) in contact with pyrrhotite and löllingite in quartz-biotite metagreywacke ranges from 35.44 to 36.45 (% atm), yielding a temperature of 360 to 475°C based on geothermometer of Sharp et al. (1985).

TABLE 5

ACCEPTED MANUSCRIPT

Hydrothermal alteration

Various styles of hydrothermal alteration are observed in association with the mineralized envelope (Fig. 11 and 13). We summarize the hydrothermal alteration type into six types including biotitization, tourmalinization, calc-silicate alteration, sericitization and chloritititization-carbonatization.

Biotitization

The most typical alteration type is biotitization which represented 70-80% of the alteration assemblage within mineralized envelope (Fig. 13a). Biotite sheets (Bt_2) defined elongated replacements zones, associated with subautomorph clinozoisite crystals (10-15%) developed on primary feldspars (10 to 40% of the whole rock) that contrasts with smaller euhedral biotite crystals (Bt_1). Three biotite generations (Table 6) are defined: 1) euhedral phlogopite grains (Bt_1) characterized by a X_{Mg} from 0.543 to 0.585 and TiO_2 content from 1.33 to 1.68 wt.% (Fig. 13b and d); 2) xenomorphic sheets of phlogopite in the matrix (Bt_2; Fig. 13a) with low X_{Mg} (0.37) and high TiO_2 (2.40 wt.%); and 3) phlogopite (Bt_3) within quartz-carbonate-gold veins, with X_{Mg} ranging from 0.558 to 0.583 and TiO_2 content ranging from 1.28 to 1.51 wt.% (Fig. 12d). Bt_2 is paragenetically later than Bt_1 (Bt_2 is associated with tourmaline and sulfides), is partially chloritized, and associated with sulfides and clinozoisite. Bt_2 phlogopite grains define a weakly penetrative schistosity. This alteration type is commonly overprinted by a chlorite-carbonate alteration assemblage.

TABLE 6

Tourmalinisation

More rarely (5-10% of alteration assemblage), tourmalinisation is developed in aluminosilicate-bearing greywacke and within strongly altered quartz-biotite or lithic greywacke. Primary tourmaline (Tur_1) are locally present (rare to 5%) in the quartz-rich matrix of aluminosilicate-bearing greywacke (Fig. 6a) as rounded grains (<10 µm). Analysed tourmaline grains (Tur_2) have composition of Mg-foitite (Table 7) and can contain sulfide inclusions (50-100 µm), quartz and apatite inclusions. Locally, a porphyroblastic texture represented by tourmaline crystals (Tur_2) ranging in size from 50 to 600 µm are developed. The matrix is dominated by biotite

ACCEPTED MANUSCRIPT

(Bt_2), chlorite (Chl_2), clinozoisite, titanite, sulfide, carbonate and plagioclase. Tourmaline grains (Tur_2) have a various composition including dravite, to uvite to Mg-Foitite composition (Table 7) with X_{Fe} ranging from 0.20 to 0.72 and TiO_2 content ranging from 0.17 to 1.09 wt.%. Biotite grains are typically phlogopitic with X_{Mg} ranging from 0.59 to 0.60 and TiO_2 content ranging from 1.00 to 1.15 wt.%.

TABLE 7

Calc-silicate alteration

Calc-silicate alteration is related to hydrothermal brecciation and veining network during DK_3 hydrothermal event (Fig. 11b, c). Actinolite, clinozoisite and carbonate are located in replacement zones associated with destabilization of feldspars while diopside (20-50 µm) is located within silica flooding (Fig. 11b) or quartz veins (Fig. 11c). The increasing proportion of DK_3 calc-silicate veinlets and silicification form hydrothermal breccia with altered pelitic clasts (Fig. 11b).

Sericitization

Sericitization is developed in aluminosilicate-bearing greywacke (45 to 75% of the hydrothermal mineral assemblage) and locally within the diorite intrusion (Fig. 13f). Sericite (<10 µm; Ms_2) is developed in association with the destabilization of feldspar in the greywacke matrix spatially associated with minor amount of clinozoisite (< 5%) and disseminated tourmaline or in veinlet selvages (Fig. 13c).

Chloritization-Carbonatization

Chloritization and carbonatization are associated with vein selvages (Fig. 13d) and sometimes massive alteration bands which overprinted the biotite-tourmaline alteration assemblage (Bt_2 and Tur_2; Fig. 11d and e). Characterized by millimetric to plurimillimetric sheets of chlorite commonly developed on biotite crystals (Fig. 11e and Fig 13e). These are associated with elevated gold grades ranging between 50 and 60 g/t of Au. All of the compositions measured for the chlorite (Chl_2) found in the matrix fall along the binary lines between clinochlore and corundophilite, with Si content ranging from 2.64 to 2.72 apfu and X_{Mg} ranging from 0.51 to 0.65. Chlorite

ACCEPTED MANUSCRIPT

549 grains (Chl_1) in inclusion within tourmaline crystals (Tur_2) have higher Si content ranging from 2.73 to 2.94 apfu
550 and X_{Mg} ranging from 0.63 to 0.66.
551
552 **FIGURE 13**

553 ## Geochronology

554
555 *U-Pb dating of the KDH337 diorite*
556
557 More than 50 zircon grains were separated for LA-ICPMS U-Pb dating of the diorite intrusion. They are
558 characterized by subeuhedral shapes and sizes ranging from 100 to 200 μm (Fig. 14). Twenty-two grains were
559 analyzed (Table 8). Fifteen of them (±1% of discordancy; italic in Table 8) yield a concordia age of 2140.4 ± 7.2
560 Ma (MSWD = 2; n = 15) that we interpret as the emplacement age for this diorite. If all the data are taken into
561 account, we end up with a similar, weighted average $^{207}Pb/^{206}Pb$ age of 2140.1 ± 7.9 Ma (MSWD = 0.42, n =
562 22).
563
564 **FIGURE 14**
565 **TABLE 8**
566
567 *Re-Os dating on pyrrhotite*
568
569 In order to provide geochronological constraints on the mineralizing events, pyrrhotite crystals were selected for
570 Re-Os dating. However, close association between electrum, pyrrhotite and other sulfides (chalcopyrite,
571 arsenopyrite) in zones presenting evidences of reworking and remobilization (Fig. 12a, b and c) made it difficult
572 to obtain pure mineral separates, which may impact on the accuracy of the ages. The effect of other sulfide
573 phases was minimized by selecting the sample KDH280-101 m, contains the least amount of chalcopyrite and
574 pyrite (<5% of sulfides phases) compared to pyrrhotite. DK_2-foliated pyrrhotite grains associated with low-grade
575 gold mineralization in quartz-biotite metagreywackes were analyzed in order to constrain the age of the early
576 gold mineralization event.
577 Results of the Re-Os dating of pyrrhotite grains are given in Table 8. The ^{187}Re contents of the analyzed
578 pyrrhotites are around 2.3-2.4 ppb, while ^{187}Os varies from 54.4 to 57.4 ppt. In all cases, more than 99% of the

ACCEPTED MANUSCRIPT

measured ^{187}Os is radiogenic in nature, based on the measured ^{188}Os content and assuming a common $^{187}Os/^{188}Os$ ratio of 0.5±0.4. As it was impossible to constrain the initial $^{187}Os/^{188}Os$ ratio directly from the data, this value was chosen to include potential common Os compositions ranging from mantle to crustal values at 2 Ga. As nearly all of the Os is radiogenic in nature, Re-Os ages can be calculated from individual samples. Three replicates yield reproducible dates between 2168 and 2150 Ma, and provide a weighted average date of 2157 ± 24 Ma (MSWD = 2.5; n = 3). If the Os in the pyrrhotite is derived from a mantle source, the age would be close to the upper limit of this range.

TABLE 9

Discussion

Key features and implications for exploration

This study is the first detailed description of the local geology associated with the Kiaka gold deposit. Major insights are linked to four key observations, including: i) cross-cutting hydrothermal alteration with distinct styles and mineral assemblages, ii) the close spatial link between D_2-related fold hinges and/or shear zones and gold distribution (Fig. 4b. c and d), iii) the lithic greywacke and/or the quartz-biotite greywacke (Fig. 5), as preferential host rocks for disseminated-style of gold mineralization (Fig. 4, Fig. 11a), and iv) the mineralized contacts between contrasting lithologies such as quartz-biotite metagreywackes, aluminosilicate-bearing metapelites, gabbro, and orthopyroxene-garnet schist. Shear zone intersection (N-S and N-trending) and the association with lithological boundaries are also potentially critical for exploration as those features are ubiquitous in the Kiaka gold deposit (e.g. hinges illustrated by the lithic greywacke geometry, contact between garnet-orthopyroxene-bearing schist and lithic greywacke and/or D_2-related shear zone).

Located in the north part of the ore bodies, the Kiaka diorite shows evidence of local shearing (D_2-related), record a retrogression overprint and chlorite-carbonate alteration assemblage with minor amount of pyrrhotite and chalcopyrite supporting its emplacement before D_3 or D_4 hydrothermal events. No clear relationship with the stage 1 of mineralization and the diorite intrusion is observed but some small ore bodies appear to cut across or developed at the contact with small dioritic dykes (Fig.4a). Our data supports close spatial and temporal

relationships between deformation (D_2, D_3 and D_4), gold, diorite magmatism and amphibolite facies metamorphism, a feature also described in the Baoulé-Mossi domain (John et al. 1999; Debat et al. 2003; Ganne et al. 2011; McFarlane et al., 2011), in the Trans Hudson orogen (Lawley et al., 2016) and the Lupa goldfield (Lawley et al., 2013).

New insights into the timing of gold mineralization

Re-Os dating of syn-SK_2 xenomorphic pyrrhotite (possibly mixed with some chalcopyrite and arsenopyrite) yields a weighted average Re-Os age of 2157 ± 24 Ma (MSWD=0.25; n=3). At microscopic scale, sulfides are often stretched along the metamorphic SK_2 foliation (Fig. 11a), and sometimes remobilized in pressure shadows of sillimanite-kyanite porphyroblasts (Fig. 12a). These petrographic observations suggest that pyrrhotite, together with biotite, are associated with the pre- to early-SK_2 gold mineralization. Thus, this date also provides a minimum age constrain on the early mineralizing event at ca. 570°C supported by the presence of pyrrhotite, arsenopyrite and löllingite in equilibrium. However, Re-Os data on pyrrhotite grains have to be interpreted with caution because of the low closing temperature for this mineral in association with rhenium and osmium diffusion within pyrrhotite crystals (300 – 400 °C, Brenan et al. 2000). This age suggests an early lode gold event during the Eburnean orogeny at ~2150 Ma as proposed in other lode gold deposit through the West African Craton (Le Mignot et al., 2016b). The late gold endowment associated with DK_3 and DK_4 may be related to the early or the later lode gold event described at ~2100-2040 Ma at the Wassa (Perrouty et al. 2015, Parra-Avila et al. 2015, Le Mignot et al. 2016b), Damang (Pigois et al. 2003, White et al. 2014), Obuasi (Milesi et al. 1992, Allibone et al. 2002, Fougerouse et al. 2016), Loulo (Lawrence et al. 2013 ; Lambert-Smith et al., 2016a and b), and Nassara deposits (Ouiya et al. 2015, Le Mignot et al. 2016b). The two gold events described here in Kiaka illustrate the polyphase character of the Paleoproterozoic gold mineralization (Lawrence et al., 2013, Eglinger et al., 2015, Le Mignot et al., 2016b). This polyphase character has been described throughout the West African Craton, but also in other Proterozoic orogenic gold districts as in the Churchill province (Lawley et al., 2016); in the Ubendian belt (Lawley et al., 2013; Kazimoto et al. 2015) and in the Guyana shield (Daoust et al., 2011).

The onset of the Eburnean orogeny (~2150 Ma) is a critical period where early-structures (~2160 Ma) were potentially reactivated in reverse shear zones and act as major pathways for gold-bearing fluids. The Markoye

ACCEPTED MANUSCRIPT

shear zone is an important metallotect for gold as at least two world-class gold deposits (Essakhane and Kiaka, Fig. 1) are located nearby (Figure 2). Our dates (Re-Os and U-Pb) are concomitant with a long-lived D_2 regional tectonic event (Fig. 16), M_2 metamorphism and magmatic activity. Interestingly, our new diorite age (2140 ± 7 Ma), which constrains the timing of D_2, is slightly younger than the weighted average Re-Os pyrrhotite age at (2157 ± 24 Ma), suggesting that the early disseminated gold stage may pre-date D_2. As the Kiaka diorite is locally deformed, we associate its emplacement with syn- or late-D_2. The nearby Kaouré (2128 ± 6 Ma; Castaing et al. 2003) and Ouargaye granites (2135± 6 Ma by U-Th-Pb on monazite; Castaing et al., 2003) are younger Z-shaped intrusions controlled and/or affected by two sinistral shear zones. We therefore suggest that transcurrent reactivations of D_2-related shear zones occured between 2140 to 2100 Ma (this study and Vegas et al. 2007) and was potentially associated with D_3 and D_4 hydrothermal circulation and higher gold grades.

FIGURE 15

FIGURE 16

Conclusion

The Kiaka gold deposit has been studied using a multidisciplinary approach including field observations, core logging, petrography, geothermobarometry, and geochronology. Four deformation events have been recognized in the local area and at least two of them play an important role in gold distribution and concentration. The key features highlighted by this study of the Kiaka gold deposit are as follows:

1. The host rocks are metamorphosed volcano-sedimentary rocks including quartz-biotite metagreywacke, lithic metagreywacke, quartz-muscovite schist, aluminosilicate-bearing metapelites and garnet-orthopyroxene schist.
2. The deposit is located at the intersection of the D1 N-S Markoye shear zone and the DK_2-related NE-trending shear zones. The latter strongly controlled the geometry of the volcano-sedimentary sequence illustrated by structures such as FK_1, FK_2 folds, DK_2-related shear bands and mineral LK_2 lineations.
3. Four subparallel elongated ore bodies are hosted by the quartz-biotite metagreywackes, aluminosilicate-bearing metapelites and the lithic metagreywackes and some is developed in an apparent axial plane of the DK_2 isoclinal folds.

ACCEPTED MANUSCRIPT

4. Hydrothermal alteration related to gold occurs as i) pervasive alteration zones dominated by biotite and clinozoizite during the DK_2 event (disseminated stage) and ii) calc-silicate monomineral or bimineral DK_3 veins and veinlets (diopside, actinolite) and DK_4 pervasive muscovite, chlorite and calcite in quartz-carbonates vein selvages (vein stage).

5. Based on crosscutting relationships, mineral assemblages and mineralization styles, two stages of gold mineralization are recognized: an early disseminated stage with pyrrhotite ± pyrite, chalcopyrite (1-3 g/t Au) and a late vein stage with pyrrhotite, arsenopyrite, electrum, native gold and tellurobismuthite (50-60 g/t Au) .

6. The emplacement of a dioritic intrusion, dated at 2140 ± 7 Ma (concordia $^{207}Pb/^{206}Pb$ age on magmatic zircon), is contemporaneous with displacement along mineralized, sinistral-reverse D_2-related shear zones. The early disseminated sulfide stage is dated at 2157 ± 24 Ma (Re-Os age), the first absolute age of Au mineralisation in the Manga Fada N'Gourma area. This could correspond to the early lode gold event in the Baoule-Mossi at ~2150 Ma.

Acknowledgements

We are grateful to Didier Kaboré, Michael Baddy Wanye and geologists from Volta Resources (now B2Gold Corp.) for logistical aid and organization that provided us with optimal conditions for fieldwork and also for authorization to publish. Discussions during field work on Burkina Faso geology with Didier Béziat, and Seta Naba greatly improved the manuscript. Lenka Baratoux (IRD in Dakar) is deeply thanked for sharing her understanding of the geology and metamorphic events during the Eburnean orogeny. Re-Os manipulations wouldn't have been possible without the technical support of Catherine Zimmerman and Christiane Parmentier. Staff from the lithopreparation lab (Cedric Demeurie and Alexandre Flammang) and SCMEM (Service Commun de Microscopies Electroniques et de Microanalyses, GeoRessources) are thanked for thin sections and imagery using the electron microprobe and SEM, respectively. The senior author would like to thank Alain Cheilletz for precious advice and suggestions for this study and Marie Lefebvre for biotite data acquisition. Finally, we are grateful to AMIRA International and industry sponsors, including AusAid and the ARC Linkage Project LP110100667, for their support on the WAXI project (P934A). This study is part of the WAXI 2 program (http://waxi2.org/). Luc Siebenaller acknowledges the Luxemburgish Fonds National de la Recherche (FNR) for the AFR post-doc grant (PDR-09-029) he benefited to conduct part of this research. Constructive and detailed

ACCEPTED MANUSCRIPT

reviews by James Lambert-Smith and Christopher Lawley greatly improve the manuscript and help to clarify many key points.

References

Abouchami, W., Boher, M, 1990. A Major 2.1 Ga Event of Mafic Magmatism in West Africa: An Early Stage of Crustal Accretion. J Geophys Res B Solid Earth and Planets 95(17):605-617

Agyei Duodu J, Loh GK, Hirdes W, Boamah KO, Baba M, Anokwa YM, Asare C, Brakohiapa E, Mensah RB, Okla R, Toloczyki M, Davis DW, Glück S (2009) Geological Map of Ghana 1:1,000,000. BGS/GGS, Accra, Ghana/Hannover, Germany

Allibone, A., Teasdale, J., Cameron, G., Etheridge, M., Uttley P., Soboh, A., Appiah-Kubi, J., Adanu, A., Arthur, R., Mamphey, J., Odoom, B., Zuta, J., Tsikata, A., Pataye, F., Famiyeh, S., Lamb, E., 2002. Timing and structural controls on gold mineralization at the Bogoso gold mine, Ghana, West Africa. Economic Geology 97, 949-969

Ama, Salah, I., Liegeois, JP., Pouclet, A., 1996. Evolution d'un arc insulaire océanique birimien précoce au Liptako nigérien (Sirba): géologie, géochronologie et géochimie. Journal of African Earth Sciences 22, 235-254

André-Mayer, AS., Ramiandrisoa, N., Vanderhaeghe, O., Reisberg, L., Rabeandrasana, S., Zimmermann, C., 2014, Re-Os geochronological constraints on the Dabolava mesothermal gold occurence, Madagascar: Implications for the Ikalamavony sub-domain deposition age. Journal of African Earth Sciences 94, 119-127

B2Gold Corp (2013) Joint News release B2Gold Corp. agrees to acquire Volta Resources Inc. (http://b2gold.mwnewsroom.com/Files/9b/9b6b423f-7a7f-4b95-a1ba-384247c09540.pdf)

Ballouard, C., Boulvais, P., Poujol, M., Gapais, D., Yamato, P., Tartèse, R., Cuney, M., 2015. Tectonic record, magmatic history and hydrothermal alteration in the Hercynian Guérande leucogranite, Armorican Massif, France. Lithos 220-223:1-22

Baratoux, L., Metelka, V., Naba, S., Jessell, WM., Grégoire, M, Ganne, J., 2011. Juvenile Paleoproterozoic crust evolution during the Eburnean orogeny (~2.2–2.0 Ga), western Burkina Faso. Precambrian Research 191:18-45

ACCEPTED MANUSCRIPT

726 Baratoux, L., Béziat, D., Block, S., Davis, J., Dioh, E., Fontaine, A., Ganne, J., Kennedy, K., Miller, J., Parra, L.,
727 Perrouty, S., Siebenaller, L., 2013. Thermal evolution of the Ore-bearing Birimian Provinces:
728 Unpublished Report, Module 1.4, Final Report P934A- West African Exploration Initiative-Stage 2,
729 924 p
730 Béziat, D., Bourges, F., Debat, P., Lompo, M., Martin, F., Tollon, F., 2000. A Palaeoproterozoic ultramafic-
731 mafic assemblage and associated volcanic rocks of the Boromo greenstone belt: fractionates originating
732 from island-arc volcanic activity in the West African craton. Precambrian Research 101, 25-47.
733 Béziat, D., Dubois, M., Debat, P., Nikiéma, S., Salvi, S., Tollon, F., 2008. Gold metallogeny in the Birimian
734 craton of Burkina Faso (West Africa). Journal of African Earth Sciences 50, 215-233.
735 Birck, JL., Barman, M., Capmas F (1997) Re-Os isotopic measurements at the femtomole level in natural
736 samples. Geostandards Newsletter 20, 19-27.
737 Block, S., Ganne, J., Baratoux, L., Zeh, A., Parra, LA., Jessell, M., Ailleres, L., Siebenaller, L., Mensah, E.,
738 2015. Petrological and geochronological constraints on lower crust exhumation during Paleoproterozoic
739 (Eburnean) orogeny, NW Ghana, West African craton. Journal of Metamorphic Geology 33, 463-494.
740 Boher, M., Abouchami, W., Michard, A., Albarede, F., Arndt, NT., 1992. Crustal Growth in West Africa at 2.1
741 Ga. Journal of Geophysical Research 97, 345-369.
742 Böhlke, JK., 1982. Orogenic (metamorphic-hosted) gold-quartz veins. US Geological Survey Open File Report
743 795, 70-76.
744 Bonhomme, M., 1962. Contribution à l'étude géochronologique de la plate-forme de l'Ouest africain.
745 Unpublished PhD thesis, Clermont-Ferrand, France, University of Clermont-Ferrand, 62 p.
746 Bossière, G., Bonkoungou, I., Peucat, JJ., Pupin, JP., 1996. Origin and age of Palaeoproterozoic conglomerates
747 and sandstones of the Tarkwaian Group in Burkina Faso, West Africa. Precambrian Research 80, 153-
748 172.
749 Bourassa, Y., 2003. Wassa Geology Report: Golden Star Resources Ltd, internal report, 34p;
750 Brenan, JM., Cherniak, DJ., Rose, LA., 2000. Diffusion of osmium in pyrrhotite and pyrite: implications for
751 closure of the Re-Os isotopic system. Earth Planetary Sciences Letters 180, 399-413.
752 Brugier, O., Bosch, D., Caby, R., Monié, P., 2013. Timing of Paleroproterozoic events in the Birimian of the
753 West African Craton. Unpublished report, Module 1.5, Final Report P934A- West African Exploration
754 Initiative-Stage 2, 924p.

ACCEPTED MANUSCRIPT

McCuaig, EC., Hronsky JMA. 2014. The mineral system concept: the key to Exploration targeting, Society of Economic Geologists, Inc., Special Publication 18, 153-175.

Carignan, J., Hild, P., Mévelle, G., Morel, J., Yeghicheyan, D., 2001. Routine analyses of trace elements in geological samples using flow injection and low pressure on-line liquid chromatography coupled to ICP-MS: a study of reference materials BR, DR-N, UB-N, AN-G and GH. Geostandards Newsletter 25, 187-198.

Champion, DC., Sheraton, JW., 1997. Geochemistry and Nd isotope systematics of Archaean granites of the Eastern goldfields, Yilgarn Craton: Implications for crustal growth processes. Precambrian Research 83, 109-132.

Cardon, O., Reisberg, L., André-Mayer, AS., Leroy, J., Milu, V., Zimmermann, C., 2008. Re-Os systematics of pyrite from the Bolcana porphyry copper deposit, Apuseni Mountains, Romania. Economic Geology 103, 1695-1702.

Colvine, AC., Fyon, JA., Heather, KB., Marmont, S., Smith, PM., Troop, DG., 1988. Archean Lode Gold Deposits in Ontario. Ontario Geological Survey, Miscellaneous Paper 139, 136 p.

Connolly, J.A.D., 2005. Computation of phase equilibria by linear programming: A tool for geodynamic modeling and its application to subduction zone decarbonation. Earth and Planetary Science Letters 236, 524-541.

Connolly, J.A.D., 2009. The geodynamic equation of state: what and how. Geochemistry, Geophysics, Geosystems 10:Q10014 DOI:10.1029/2009GC002540.

Cox, K.G., Bell, J.D., Pankhurst, R.J., 1979. The interpretation of igneous rocks. Allen & Unwin 464p.

Craw, D., Koons, P.O., 1989. Tectonically induced hydrothermal activity and gold mineralisation adjacent to major fault zones. Economic Geology Monograph 6, 471-478.

Creaser, R.A., White, A.J.R., 1991. Yardea-Dacite-Large volume, high-temperature felsic volcanism from the Middle Proterozoic of South Australia. Geology 19, 48-51.

Davis, D.W., Hirdes, W., Schaltegger, E., Nunoo, E.A., 1994. U/Pb age constraints on deposition and provenance of Birimian and goldbearing Tarkwaian sediments in Ghana,West Africa. Precambrian Research 67, 89-107.

Davis, J., Miller, J., Thébaud, N., McCuaig, T.C., Jessel, M., Begg, G., Hein, K., Baratoux, L., 2015. Craton-scale lithostratigraphic correlation as an insight for the geodynamic evolution of the SWAC, Proceedings 13th SGA Biennial Meeting 4, 1587-1590.

785 Debat, P., Nikiéma, S., Mercier, A., Lompo, M., Béziat, D., Bourges F, Roddaz M, Salvi S, Tollon F,
786 Wenmenga U, (2003) A new metamorphic constraint for the Eburnean orogeny from Paleoproterozoic
787 formations of the Man shield (Aribinda and Tampelga countries, Burkina Faso). Precambrian Res
788 123:47-65

789 Dioh, E., Béziat, D., Debat, P., Grégoire, M., Ngom, P.M., 2005. Diversity of the Palaeoproterozoic granitoids of
790 the Kédougou inlier (Eastern Sénégal): Petrographical and geochemical constraints. Journal of African
791 Earth Sciences 44, 351-371.

792 Doumbia, S., Pouclet, A., Kouamelan, A., Peucat, J.J., Vidal, M., Delor, C., 1998. Petrogenesis of juvenile-type
793 Birimian (Paleoproterozoic) granitoids in Central Cote-d'Ivoire, West Africa: Geochemistry and
794 geochronology. Precambrian Research 87, 33-63.

795 Drummond, M.S., Defant, M.J. 1990. A Model for trondhjemite□tonalite□dacite genesis and crystal growth via
796 slab melting: Archean to modern comparisons. Journal of Geophysical Research 95, 503-521.

797 Doublier, M.P., Thébaud, N., Wingate, M.T.D., Romano, S.S., Kirkland, C.L., Gessner, K., Mole, D.R., Evans,
798 N., 2014. Structure and timing of Neoarchean gold mineralization in the Southern Cross district
799 (Yilgarn Craton, Western Australia) suggest leading role of late Low-Ca I-type granite intrusions.
800 Journal of Structural Geology 67(B), 205-221.

801 Egal, E., Thiéblemont, D., Lahondère, D., Guerrot, C., Costea, C.A., Iliescu, D., Delor, C., Goujou, J.C., Lafon,
802 J.M., Tegyey, M., 2002. Late Eburnean granitization and tectonics along the western and northwestern
803 margin of the Archean Kenema- Man domain (Guinea West African Craton). Precambrian Research
804 117, 57-84.

805 Eglinger, A., Thébaud, N., Davis, J., Miller, J., Zeh, A., McCuaig C, Belousova E (2015) High-K to shoshonitic
806 magmatism across the northern Archean Kéména Man margin (Guinea): Implications for the Eburnean
807 orogenic gold minerlizations. Mineral Resources in a sustainable world. Proceedings 13th SGA Biennial
808 Meeting 4:1591-1594

809 Feybesse, J.L., Milési, J.P., 1994. The Archean/Proterozoic contact zone in West Africa: a mountain belt of
810 décollement thrusting and folding on a continental margin related to 2.1 Ga convergence of Archean
811 cratons? Precambrian Research 69,199-227.

812 Feybesse, J.L., Billa, M., Guerrot, C., Duguey, E., Lescuyer, J.L., Milesi, J.P., Bouchot, V., 2006. The
813 paleoproterozoic Ghanaian province: Geodynamic model and ore controls, including regional stress
814 modeling. Precambrian Research 149, 149-196.

ACCEPTED MANUSCRIPT

815 Frimmel, H.E., 2008, Earth's continental crustal gold endowment. Earth and Planetary Science Letters 267, 44-
816 55.
817 Fu, B., Touret, J.L.R., 2014, From granulite fluids to quartz-carbonate megashear zones: The gold rush.
818 Geoscience Frontiers 5, 747-758.
819 Ganne, J., De Andrade, V., Weinberg, R., Dubacq, B., Vidal, O., Kagambega, N., Naba, S., Baratoux, L., Jessell,
820 M., Allibone, J., 2011. Modern-style plate subduction pre-served in the Palaeoproterozoic West African
821 Craton. Nature Geosciences 5, 60-65.
822 Ganne, J., Gerbault, M., Block, S., 2014. Thermo-mechanical modeling of lower crust exhumation-Constraints
823 from the metamorphic record of the Palaeoproterozoic Eburnean orogeny, West African Craton.
824 Precambrian Research 243, 88-109.
825 Gasquet, D., Barbey, P., Adou, M., Paquette, J.L., 2003. Structure, Sr-Nd isotope geochemistry and zircon U-Pb
826 geochronology of the granitoids of the Dabakala area (Côte d'Ivoire): evidence for a 2.3 Ga crustal
827 growth event in the Palaeoproterozoic of West Africa. Precambrian Research 127, 329-35.
828 Goldfarb, R.J., Groves, D.I., Gardoll S., 2001. Orogenic gold and geologic time: a global synthesis. Ore Geology
829 Reviews 18, 1-75.
830 Goldfarb, R., Baker, T., Dubé, B., Groves, D.I., Hart, C.J.R., Gosselin, P., 2005. Distribution, Character, and
831 Genesis of Gold Deposits in Metamorphic Terranes. Economic Geology 100th Anniversary Volume
832 Groves, D.I., Goldfarb, R.J., Robert, F., Hart, C.J.R., 2003. Gold deposits in Metamorphic Belts: Overview of
833 Current Understanding, Outstanding Problems, Future Research and Exploration Significance.
834 Economic Geology 98, 1-29.
835 Hammarstrom JM, Zen E (1986) Aluminium in hornblende: an empirical igneous geobarometer. American
836 Mineralogist 71:1297-1313
837 Hein, K.A.A., 2010. Succession of structural events in the Goren greenstone belt (Burkina Faso): implications
838 for West African tectonics. Journal of African Earth Sciences 56, 83-94.
839 Henry, D.J., Guidotti, C.V., Thomson, J.A., 2005. The Ti-saturation surface for low-to-medium pressure
840 metapelitic biotites: Implications for geothermometry and Ti-substitution mechanisms. American
841 Mineralogist 90, 316-328.
842 Hirdes, W., Davis, D.W., Eisenlohr, B.N., 1992. Reassessment of Proterozoic granitoid ages in Ghana on the
843 basis of U/Pb zircon and monazite dating. Precambrian Research 56, 89-96.

ACCEPTED MANUSCRIPT

Hirdes, W., Davis, D.W., Lüdtke, G., Konan, G.,1996. Two generations of Birimian (Paleoproterozoic) volcanic belts in northeastern Côte d'Ivoire (West Africa): consequences for the «Birimian controversy». Precambrian Research 80, 173-191.

Hirdes, W., Davis, D.W., 1998. First U-Pb zircon age of extrusive volcanism in the Birimian Supergroup of Ghana/West Africa. Journal of African Earth Sciences 27, 291-294.

Holland, T. J. B. and Powell, R., 1998. An internally consistent thermodynamic data set for phases of petrological interest. Journal of Metamorphic Geology, 16, 309-343.

Hollister LS, Grisson GC, Peters EK, Stowell HH, Sisson VB (1987) Confirmation of the empirical correlation of Al in hornblende with pressure of solidifcation of calc-alkaline plutons. American Mineralogist 72(34):231-239

Hottin G, Ouedraogo OF (1976) Carte géologique de la République de Haute-Volta. Direction de la Géologie et des Mines, Ouagadougou, 1 feuille, notice 58 p

Hottin G, Ouedraogo OF (1992) Carte géologique du Burkina Faso, BRGM/Bureau des Mines et de la Géologie du Burkina, Ouagadougou, 1 feuille, notice 58 p

Johnson, M.C., Rutherford, M.J. 1992. Experimental calibration of the aluminum-in-hornblende geobarometer with application to Long Valley caldera (California). Geology 17, 837-841.

Kerrich R, Goldfarb R, Groves D, Garwin D (2000) The geodynamic of world-class gold deposits: characteristics, space-time distribution and origins, in Hagemann SG, Brown PE (eds) Gold in 2000. Society of Economic Geologists, Reviews in Econ Geol 13:501-551

Klockner, I.A., 1991. Cartographie géologie du sillon de Téra, Etude géochronologique. Unpublished report, Ministry of Mines and Energy of Niger, Niamey 49-59.

Koons, P.O., Craw, D., 1991. Gold mineralization as a consequence of continental collision: an example from the Southern Alps, New Zealand. Earth Planetary Sciences Letters 103, 1-9.

Kretschmar, U., Scott, S.D., 1976. Phase relations involving arsenopyrite in the system Fe-As-S and their application. The Canadian Mineralogist 14, 364-3.

Lambert-Smith, J.S., Lawrence D.M., Müller W., Treloar P.J., 2016a, Palaeotectonic setting of the south-eastern Kédougou-Kéniéba Inlier, West Africa: New insights from igneous trace element geochemistry and U-Pb zircon ages, Precambrian Research 274, 110-135.

ACCEPTED MANUSCRIPT

Lambert-Smith, J.S., Lawrence, D.M., Vargas, C.A., Boyce, A.J., Treloar, P.J., The Gounkoto Au deposit, West Africa: Constraints on ore genesis and volatile sources from petrological, fluid inclusion and stable isotope data, Ore Geology Reviews 78, 606-622.

Lanari, P., Wagner, T., Vidal, O., 2014. A thermodynamic model for di-trioctahedral chlorite from experimental and natural data in the system MgO-FeO-Al_2O_3-SiO_2-H_2O: applications to P-T sections and geothermometry. Contributions to Mineralogy and Petrology 167, 968.

Large, R.R., Bull, S.W., Maslennikov, V., 2011. A carbonaceous sedimentary source-rock model for Carlin-type and orogenic gold deposits. Economic Geology and the Bulletin of the Society of Economic Geologists 106, 331-358.

Lawley, C.J.M., Selby, D., Condon D.J., Horstwood M., Millar, I., Crowley Q., Imber J., 2013. Lithogeochemistry, geochronology and geodynamic setting of the Lupa Terrane, Tanzania: implications for the extent of the Archean Tanzanian Craton, Precambrian Research 231, p. 174-193.

Lawley C.J.M.m McNicoll V., Sandeman H., Pehrsson S., Simard M., Castonguay S., Mercier-Langevin P., Dubé B., 2016. Age and geological setting of the Rankin Inlet greenstone belt and its relationships to the gold endowment of the Meliadine gold district, Nunavut, Canada. Precambrian Research 275, p. 471-495.

Lawrence, D.M., Treolar, P.J., Rankin AH, Harbidge P, Holliday J (2013) The geology and mineralogy of the Loulo mining district, Mali, West Africa: Evidence for two distinct styles of orogenic gold mineralization. Econ Geol 108:199-227.

Le Métour, J., Chèvremont. P., Donzeau, M.E., Thiéblemont, E., Tegey, D., Guerrot, M.C., Itard, B., Castaing, Y., Delpont, C., Ki, G., Zunino, J.C.C., 2003. Notice explicative de la Carte géologique du Burkina Faso à 1/200,000. Feuille Houndé 82p.

Le Mignot, E., 2014, Les gisements d'or comme témoins de l'histoire géologique du craton ouest-africain : Apports de la datation

Le Mignot, E., Siebenaller, L., Béziat, D., André-Mayer, A-S., Reisberg, L., Salvi, S., Vélasquez, G., Zimmermann, C., Naré, A., 2016a. The Paleoproterozoic copper-gold deposit at Gaoua, Burkina Faso: Superposition of orogenic gold on porphyry copper mineralization. Economic Geology, accepted

Le Mignot, E., Reisberg, L., André-Mayer, A-S., Bourassa, Y., John, M., 2016b. Re-Os geochronological evidence for multiple Paleoproterozoic gold events at the scale of the West African craton. Economic Geology, accepted.

ACCEPTED MANUSCRIPT

902 Leube, A., Hirdes, W., Mauer, R., Kesse, G.O. 1990. The early proterozoic birimian supergroup of Ghana and
903 some aspects of its associated gold mineralization. Precambrian Research 46, 139-165.
904 Lindgren, W. 1933. Mineral deposits. 4th ed New York McGraw-Hill, 930p.
905 Lompo, M., 1991. Etude structurale et géologique des séries birimiennes de la région de Kwademen, Burkina
906 Faso, Afrique de l'Ouest. Doctorat de l'université de Clermont Ferrand, France 192p.
907 Lompo, M., 2009. A model of subsidence of an oceanic plateau magmatic rocks in the Man-Leo Shield of the
908 West African Craton Geodynamic evolution of the 2.25–2.0 Ga Palaeoproterozoic. In: Reddy SM,
909 Mazumder R, Evans DAD, Collins AS (Eds) Palaeoproterozoic Supercontinents and Global Evolution.
910 Geological Society London 231-254.
911 Lüdtke, G., Hirdes, W., Konan, G., Kone, Y., Yao, C., Diarra, S., Zamble, Z., 1998, Geologie de la région Haute
912 Comoe Nord avec carte géologique 1/100,000. Feuilles Kong. 4B, 4d, et Tehini-Bouna 3a–3d. Bulletin.
913 No. 1 DG Abidjan, p. 178.
914 Lüdtke, G., Hirdes, W., Konan, G., Koné, Y., N'Da, D., Traoré, Y., Zamblé, Z.B., 1999. Géologie de la région
915 haute comoé sud. Carte géologique à 1/100000, feuilles dabakala 2b,d et 4b,d - 1ère édition. Projet de
916 coopération géologique ivoiro-allemenande cgia (1995-1996). Ministère des Ressources Minières et
917 Pétrolières, Direction de la Géologie, Bulletin n°2.
918 Lü, L., Mao, J., Li, H., Pirajno, F., Zhang, Z., Zhou, Z., 2011. Pyrrhotite Re-Os and SHRIMP zircon U-Pb dating
919 of the Hongqiling Ni-Cu sulfide deposits in Northeast China. Ore Geology Reviews 43, 106-119.
920 Markey, R., Stein, H.J., Hannah, JL., Zimmerman, A., Selby, D., Creaser, R.A., 2007, Standardizing Re-Os
921 geochronology: a new molybdenite Reference Material (Henderson, USA) and the soichiometry of Os
922 salts. Chemical Geology 244, 74-87.
923 Martin, H., Smithies, RH., Rapp, S., Moyen, JF., Champion, D., 2005. An overview of adakite, tonalite-
924 trondhjemite-granodiorite (TTG), and sanukitoid: relationships and some implications for crustal
925 evolution. Lithos 79, 1-24.
926 Mathur, R., Titley, S., Ruiz, J., Gibbins, S., Friehauf K., 2005. A Re-Os isotope study of sedimentary rocks and
927 copper-gold ores from the Ertsberg District, West Papua, Indonesia. Ore Geology Reviews 26, 207-226.
928 McDonough, WF., Sun, SS., 1995, The Composition of the Earth. Chemical Geology 120, 223-253.
929 McFarlane, CRM., Mavrogenes, J., Lentz, D., King, K., Allibone, A., Holcombe, R., 2011. Geology and
930 Intrusion-Related Affinity of the Morila Gold Mine, Southeast Mali. Economic Geology 106, 727-750.

McCuaig, C., Miller, J., Parra, L., Hein, K., Jessell, M., Davis, J., 2014, Craton to Regional-scale analysis of the Birimian of West Africa, Precambrian Research, Volume 274, March 2016, Pages 1-2

McCuaig, T. C., & Hronsky, J. M. (2014). The mineral system concept: the key to exploration targeting. Society of Exploration Geologists Special Publication, 18, 153-175.

Metelka, V., Baratoux, L., Naba, S., Jessell, WM., 2011. A geophysically constrained litho-structural analysis of the Eburnean greenstone belts and associated granitoid domains, western Burkina Faso. Precambrian Research 190, 48-69.

Milesi, J.P., Feybesse, J.L., Ledru, P., Dommanget, A., Ouedraogo, M.F., Marcoux, E., Prost, A., Vinchon, Ch., Sylvain, J.P., Johan, V., Tegyey, M., Calvez, J.Y. and Lagny, P. 1989. West African gold deposits in their Lower Proterozoic lithostructural setting. Chroniques Recherche Min 497, 98 pp.

Milesi, JP., Ledru, P., Feybbesse, JL., Dommanget, A., Marcoux, E., 1992. Early Proterozoic ore deposits and tectonics of Birimian orogenic belt, West Africa. Precambrian Research 58, 305-344.

Milesi JP, Feybesse JL, Pinna P, Deschamps Y, Kampunzu H, Muhongo S, Lescuyer JL, Le Goff E, Delor C, Billa M, Ralay F, Henry C (2004) Geological map of Africa 1:10,000,000. SIGAfrique project. In: 20th Conference of African Geology, BRGM, Orléans, France, 2-7 June http://www.sigafrique.net

Naba, S., Lompo, M., Debat, P., Bouchez, JL., Béziat, D., 2003. Structure and emplacement model for late-orogenic Paleoproterozoic granitoids: the Tenkodogo-Yamba elongate pluton (Eastern Burkina Faso). Journal of African Earth Sciences 38, 41-57.

Naba, S., 2007. Propriétés magnétiques et caractères structuraux des granites du Burkina Faso oriental (Craton Ouest African, 2.2-2.0Ga) : implications géodynamiques. Doctorat de l'Université de Toulouse, 175p.

Nesbitt, BE., Murowchick, JB., Muehlenbachs, K., 1986. Dual origins of lode gold deposits in the Canadian Cordillera. Geology 14, 506-509.

Neumayr, P., Ridley, JR., McNaughton, NJ., Kinny, PD., Barley, ME., Groves, DI., 1998. Timing of gold mineralization in the Mt York district: Pilgangoora greenstone belt, and implications for the tectonic and metamorphic evolution of an area linking the western and eastern Pilbara Craton, Precambrian Research 88, 249-265.

Nier, A.O. (1937) The isotopic constitution of osmium, Phys. Rev. 52, P. 885

Nier, A.O.,1950. A re-determination of the relative abundances of the isotopes of carbon, nitrogen, oxygen, argon and potassium. Physical Review. 77, 789–793.

ACCEPTED MANUSCRIPT

960 Oberthür, T., Vetter, U., Davis, DW., Amanor, JA., 1998. Age constraints on gold mineralization and
961 Paleoproterozoic crustal evolution in the Ashanti belt of southern Ghana. Precambrian Research 89,
962 129-143 .
963 Parra-Avila, L.A. Belousova, E., Fiorentini, M.L., Baratoux, L., Davis, J., Miller, J., McCuaig, T.C., 2016.
964 Crustal evolution of the Paleoproterozoic Birimian terranes of the Baoulé-Mossi domain, southern West
965 African craton: U-Pb and Hf-isotope studies of detrital zircons. Precambrian Research 274, pp. 25-60.
966 Perrouty, S., Aillères, L., Jessell, MW., Baratoux, L., Bourassa, Y., Crawford, B., 2012. Revised Eburnean
967 geodynamic evolution of the gold-rich southern Ashanti Belt, Ghana, with new field and geophysical
968 evidence of pre-Tarkwaian deformation. Precambrian Research 204-205, 12-39.
969 Perrouty, S., Jessell, MW., Bourassa, Y., Miller, J., Apau D., Siebenaller, L., Velasquez, G., Baratoux, L.,
970 Aillères L., Béziat D., Salvi S., 2015. The Wassa deposit: A poly-deformed orogenic gold system in
971 southwest Ghana – Implications for regional exploration, Journal of African Earth Sciences 112,536-
972 547.
973 Pigois, JP., Groves, DI., Fletcher, IR., McNaughton, NJ., Snee, LW., 2003. Age constraints on Tarkwaian
974 palaeoplacer and lode-gold formation in the Tarkwa-Damang district, SW Ghana. Mineralium Deposita
975 38, 695-714.
976 Ravenelle, JF., Dubé, B., Malo, M., McNicoll, V., Nadeau, L., Simoneau, J., 2010, Insights on the geology of the
977 world-class Roberto gold deposit, Eléonore property, James Bay area, Québec. Geological Survey
978 Canada, Current Research 2010-1.
979 Reisberg, L., Miesel, T., 2002. The Re-Os isotopic system: A review of analytical techniques. Geostandards
980 Newsletter 26(3), 249-267.
981 Schmidt, MW., 1992. Amphibole composition in tonalite as a function of pressure: an experimental calibration
982 of the Al-in-hornblende barometer. Contributions to Mineralogy and Petrology 110, 304-310.
983 Selby, D., Creaser, R.A., Hart C.J.R.R., Rombach, C.S., Thompson, J.F.H.H., Smith, M.T., Bakke, A.A.,
984 Goldfarb, R.J., 2002. Absolute timing of sulfide and gold mineralization: a comparison of Re–Os
985 molybdenite and Ar–Ar mica methods from the Tintina Gold Belt, Alaska. Geology 30, 791–794.
986 Selby, D., Creaser, RA., 2004. Macroscale NTIMS and microscale LA-MC-ICP-MS Re-Os isotopic analysis of
987 molybdenite: Testing spatial restrictions for reliable Re-Os age determinations, and implications for the
988 decoupling of Re and Os within molybdenite. Geochimica Cosmochimica Acta 68(19), 3897-3908.

ACCEPTED MANUSCRIPT

Sibson, RH., Robert, F., Poulsen, KH., 1988. High-angle reverse faults, fluid-pressure cycling, and mesothermal gold-quartz deposits. Geology 16: 551-555

Siegfried, P., De Kock, GS., Clarke, B., Agenbacht, A., Delor, C., Van Rooyen, RC., 2009. Geological map explanation – map sheet 0903D (1:100 000.: Mining Sector Support Programme. CGS, BRGM, Geoman, GSD, Accra

Simard, M., 2011. Multi évènements de déformation, de métamorphisme, d'hydrothermalisme à l'origine du gisement Lapa, Thèse de doctorat de l'Université du Québec à Chicoutimi

Siméon, Y., Delor, C., Vidal, M., Chiron, JC., Zeade, J., 1992. Mise en évidence d'un épisode tectonique tardi-éburnéen en Côte d'Ivoire. Comptes rendus RST, Toulouse. Société Géologique de Paris, p142

Smoliar, M.I., Walker, R.J., Morgan, J.W., 1996, Re-Os ages of group IIA, IIIA, IVA and IVB iron meteorites: Science, vol. 271, p.1099-1102.

Stein, HJ., Morgan, JW., Scherstén, A., 2000. Re-Os dating of Low-Level Highly Radiogenic sulfides: The Harnäs gold deposit, southwest Sweden, records continental-scale tectonic events. Economic Geology 95, 1657-1671.

Tapsoba B, Lo CH, Jahn BM, Chung SL, Wenmenga U, Iizuka Y (2013) Chemical and Sr–Nd isotopic compositions and zircon U–Pb ages of the Birimian granitoids from NE Burkina Faso, West African Craton: implications on the geodynamic setting and crustal evolution. Precambrian Research 224, 364-396.

Taylor, PN., Moorbath, S., Leube, A., Hirdes, W., 1992. Early Proterozoic crustal evolution in the Birimian of Ghana: constraints from geochronology and isotope geochemistry. Precambrian Research 56, 97-111.

Thomas, E., De Kock, GS., Baglow, N., Viljoen, J., Siaka, Z., 2009. Geological map explanation—map sheet 0903D (1:100,000). CGS/BRGM/Geoman. Geological Survey Department of Ghana (GSD)

Tomkins, AG., Mavrogenes, JA., 2002. Mobilization of gold as a polymetallic melt during pelite anatexis at the Challenger gold deposit, South Australia: a metamorphosed Archean deposit. Economic Geology 97, 1249-1271.

Tshibubudze, A., Hein, KAA., Marquis, P., 2009. The Markoye shear zone in NE Burkina Faso. Journal of African Earth Sciences 55, 245-256.

Tshibubudze, A., Hein, KAA., 2013. Structural setting of gold deposits in the Oudalan-Gorouol volcano-sedimentary belt east of the Markoye shear zone, West African Craton, Journal of African Earth Sciences 80, 31-47.

ACCEPTED MANUSCRIPT

1019 Tshibubudze A, Hein KAA (2015) Gold mineralization in the Essakane goldfield in Burkina Faso, West African
1020 craton. Ore Geology Reviews Rev, in press.
1021 Van Achterbergh E, Ryan CG, Jackson SE, Griffin WL (2001) Data reduction software for LA–ICP–MS:
1022 appendix. In: Sylvester PJ (ed) Laser ablation-ICP-mass spectrometry in the earth sciences: principles
1023 and applications. Mineralogical Association of Canada, Ottawa, pp 239–243
1024 Vegas N, Naba S, Bouchez JL, Jessell M (2007) Structure and emplacement of granite plutons in the
1025 Palaeoproterozoic crust of Eastern Burkina Faso: rheological implications. International Journal of
1026 Earth Sciences (Geol Rundsch) 97, 1165-1180.
1027 Vidal, M., Delor, C., Pouclet, A., Siméon, Y., Alric, G., 1996. Evolution géodynamique de l'Afrique de l'Ouest
1028 entre 2,2 Ga et 2 Ga: le style “archéen” des ceintures vertes et des ensembles sédimentaires birimiens du
1029 nord-est de la Côte-d'Ivoire. Bulletin de la Société Géologique de France 167(3), 307-319.
1030 Völkening, J., Walczyk, T., Heumann, KG, 1991. Osmium isotope ratio determinations by negative thermal
1031 ionization mass spectrometry. International Journal of Mass Spectrometry and Ion Processes 105:147-
1032 159
1033 Weatherley D.K., Henley R.W., 2013. Flash vaporization during earthquackes evidenced by gold deposits.
1034 Nature Geoscience 6, 294-298.
1035 Yavuz, F. 2007. WinAmphcal: A Windows program for the IMA-04 amphibole classification. Geochem
1036 Geophys Geosys 8:1
1037 Yavuz, F., Yavuz, V., Sasmaz, A. 2006. WinClastour-a Visual Basic program for tourmaline formula calculation
1038 and classification. Computers & Geosciences 32, 1156-1168

ACCEPTED MANUSCRIPT

ACCEPTED MANUSCRIPT

Table captions

Table 1: Major element composition of whole-rock samples analyzed by ICP-OES and traces elements composition analyzed by ICP-MS. N: Normalization on chondrite (McDonough and Sun, 1995). Samples from the Tenkodogo-Yamba batholith (T15, DD17) is analyzed by Naba et al., 2003 while basement (TC97) is from Vegas et al., 2008. Finally, Morila diorites samples are from McFarlane et al., 2011.

Table 2: Representative chemical composition of chlorite generations and thermometry from the ore zones and host rocks, by electron microprobe analysis

Table 3: Mineral analyses of amphibole grains from the Kiaka diorite (KDH337 44.1 and KDH337 69.6) by electron microprobe analyses; P1, P2, P3 and P4 refer to four geobarometers (Hammarstrom and Zen, 1986; Hollister et al., 1987; Johnson and Rutherford, 1989 and Schmidt, 1992) and mineral calculation is performed using WinAmphCal (Yavuz et al., 2007).

Table 4: Representative chemical composition of metamorphic assemblage of the garnet-orthopyroxene-bearing schist by electron microprobe analysis.

Table 5: Representative EDS analyses of ore-bearing phases in main ore bodies and alteration haloes at Kiaka.

ACCEPTED MANUSCRIPT

Table 6: Representative chemical composition of biotite generations from the ore zones and host rocks by electron microprobe analysis

Table 7: Representative chemical composition of tourmaline associated with early mineralization phase in sedimentary and volcanic protoliths. Note that stoichiometry is calculated using the WinClastour software (Yavuz et al., 2006); calculated from the normalization schemes used by the program; T, Z, Y and W refer to site positions.

Table 8: U-Pb LA-ICP-MS data for the diorite KDH337-105.5 m^{1}.

Table 9: Re-Os data for pyrrhotites from assemblages in quartz-biotite metagreywacke,

ACCEPTED MANUSCRIPT

ACCEPTED MANUSCRIPT

Table 1

Location	The Kiaka deposit				Tenkodogo		Fada-N'Gourma	Morila	Morila
Sample	KDH291-56.2	KDH75-64.9	KDH348-44.5	KDH337-44.1	T15	DD17	FC97	MANU-125	MANU-126
Rock type	volcanic rock	schist	metagreywacke	diorite	granitoid	granitoid	granitoid	diorite	diorite
Oxides / wt.%									
SiO_2	34.88	78.01	71.66	57.32	59.21	55.96	60.49	57.70	61.30
TiO_2	0.84	0.03	0.53	0.75	0.69	0.68	0.63	0.64	0.50
Al_2O_3	16.62	13.55	15.14	16.59	16.14	17.54	17.98	15.80	16.40
Fe_2O_3	15.30	0.98	3.66	7.38	5.99	7.04	5.29	7.97	6.86
MnO	0.26	0.03	0.03	0.11	0.08	0.08	0.07	0.13	0.12
MgO	10.46	< L.D.	0.97	3.90	3.41	4.36	2.75	5.18	4.01
CaO	9.55	0.56	0.77	6.57	5.59	7.27	5.69	6.64	5.16
Na_2O	0.73	4.84	1.76	3.75	4.36	4.03	4.68	2.31	1.87
K_2O	3.61	1.41	1.85	1.97	2.11	1.48	1.38	2.16	2.72
P_2O_5	0.19	< L.D.	0.14	0.27	0.34	0.29	0.28	0.38	0.19
LOI	6.12	0.86	2.74	1.53	1.00	1.02	0.69	-	-
Total	98.56	100.27	99.24	100.14	98.92	99.75	99.93	98.91	99.13
K_2O/Na_2O	4.93	0.29	1.05	0.53	0.48	0.37	0.29	0.94	1.45
A/CNK	1.20	1.99	3.46	0.82	0.82	0.82	1.53	1.42	1.68
Mg#	0.41	-	0.21	0.55	0.57	0.59	0.34	0.39	0.37
Trace elements / ppm									
Rb	107.90	48.34	44.58	51.70	66.00	52.00	84.20	5.20	5.20
Ba	1206.00	29.20	464.20	665.00	1512.00	521.00	649.00	1.00	864.00
Nb	1.39	20.32	4.16	4.29	9.15	4.01	3.14	14.30	5.34
Ta	0.10	2.09	0.41	0.33	0.63	0.31	0.155	0.20	0.33
Sr	472.80	92.33	243.70	748.00	817.00	510.00	1102.00	1102.00	687.00
Zr	56.46	104.40	117.50	129.00	275.00	144.00	103.00	2.60	135.00
Y	25.83	117.20	12.57	16.00	30.30	14.50	10.40	69.80	11.90
Hf	1.59	6.89	3.54	3.30	6.00	3.50	2.50	1.50	3.00
Ni	95.87	< L.D.	21.53	25.20	51.00	101.00	22.50	262.00	46.60
Cr	222.00	7.78	45.77	96.10	106.00	246.00	30.30	223.00	209.00
V	268.00	< L.D.	89.47	140.00	114.00	136.00	96.10	3836.00	189.00
U	0.38	5.70	1.24	1.15	1.30	1.07	0.33	0.24	1.13
Th	0.62	10.37	2.60	3.83	1.88	2.59	0.36	12.50	4.09
La	10.65	3.90	14.72	26.20	30.70	18.40	20.70	3.60	33.30
Ce	28.74	12.56	31.87	54.50	69.90	39.00	44.10	991.00	61.30
Nd	18.69	11.45	15.76	25.30	37.30	17.60	23.40	56.5	25.00
Sm	3.86	11.45	3.16	4.63	7.17	3.55	4.25	6.90	4.11
Eu	1.12	0.12	0.85	1.34	2.01	1.15	1.36	28.60	1.20
Gd	3.81	11.76	2.62	3.72	5.65	2.87	2.98	5.30	3.67
Dy	4.14	17.20	2.32	2.91	4.90	2.49	2.06	4.60	2.32
Er	2.72	10.86	1.30	1.48	2.85	1.34	0.94	0.50	1.28
Yb	3.02	11.17	1.36	1.48	2.67	1.35	0.86	2.80	1.27
Lu	0.49	1.66	0.22	0.23	0.44	0.21	0.12	1.50	0.21
Sr/Y	18.3	0.79	19.39	47.00	27.00	35.00	106.00	15.79	57.73
La/Yb	3.52	0.35	10.82	18.00	12.00	14.00	24.00	1.00	26.00
Y/Yb	8.54	10.49	9.24	11.00	11.00	11.00	12.00	25.00	9.00
$(La/Yb)_N$	-	-	-	13.00	8.00	10.00	35.00	1.00	18.00

ACCEPTED MANUSCRIPT

ACCEPTED MANUSCRIPT

Table 2

Sample	KDH291-56.2										
Analyses	ZM-10-24b	ZM-10-24b	ZM-10-24b	ZM-10-24b	c1-2a	c1-2b	c1-2c	c1-2d	c3-1a	c3-1b	c3-1c
Mineral	Chl1	Chl1	Chl1	Chl1	Chl2	Chl2	Chl2	Chl2	Chl2	Chl2	Chl2
Location	Inc. tur	Inc. tur	Inc. tur	Inc. tur	Matrix	Matrix	Matrix	Matrix	Matrix	Matrix	Matrix
Oxides (wt.%)											
SiO_2	27.71	25.76	26.75	26.10	26.66	26.35	26.69	26.77	26.34	25.78	26.49
TiO_2	0.06	0.01	0.04	0.13	0.04	0.02	0.04	0.01	0.00	0.03	0.05
Al_2O_3	18.83	18.34	18.20	19.12	21.68	21.72	21.41	21.38	21.66	20.35	21.93
FeO	24.83	24.58	24.64	25.26	20.71	20.02	20.72	20.58	20.28	20.34	20.81
MnO	0.58	0.55	0.35	0.62	0.41	0.35	0.42	0.42	0.36	0.41	0.33
MgO	14.91	15.10	15.76	14.29	18.62	18.63	19.13	18.81	18.27	18.08	18.93
CaO	0.13	0.35	0.06	0.20	0.05	0.04	0.00	0.00	0.03	0.00	0.05
Na_2O	0.02	0.09	0.07	0.03	0.04	0.09	0.00	0.03	0.03	0.00	0.01
K_2O	0.66	0.08	0.11	0.00	0.00	0.07	0.13	0.09	0.03	0.08	0.07
Σ	87.73	84.86	85.98	85.75	88.21	87.29	88.54	88.09	87.00	85.07	88.67
nOx	14	14	14	14	14	14	14	14	14	14	14
Si	2.886	2.730	2.785	2.745	2.703	2.694	2.691	2.718	2.703	2.709	2.665
Al^{IV}	1.109	1.269	1.212	1.244	1.294	1.305	1.306	1.282	1.297	1.288	1.331
Al^{VI}	1.202	1.021	1.022	1.126	1.296	1.312	1.237	1.276	1.324	1.232	1.270
Ti	0.005	0.001	0.003	0.010	0.003	0.002	0.003	0.001	0.000	0.002	0.004
Fe^{2+}	1.838	1.307	1.287	1.445	1.580	1.541	1.485	1.573	1.567	1.520	1.489
Fe^{3+}	0.324	0.871	0.858	0.778	0.176	0.171	0.262	0.175	0.174	0.268	0.263
Mn	0.051	0.049	0.031	0.055	0.035	0.030	0.036	0.036	0.031	0.036	0.028
Mg	2.315	2.385	2.446	2.241	2.814	2.839	2.875	2.847	2.795	2.832	2.839
Ca	0.015	0.040	0.007	0.023	0.005	0.004	0.000	0.000	0.003	0.000	0.005
Na	0.004	0.018	0.014	0.006	0.008	0.018	0.000	0.006	0.006	0.000	0.002
K	0.088	0.011	0.015	0.000	0.000	0.009	0.017	0.012	0.004	0.011	0.009
X_{Mg}	0.56	0.65	0.66	0.61	0.64	0.65	0.66	0.64	0.64	0.65	0.66

ACCEPTED MANUSCRIPT

Table 4

Sample	KDH337 (44.1 and 69.6)									
Analysis		c3-1	c4-3	c4-4	c3-3	c1-3	c3-2	c2-5	c5-1	
Minerals	Plagiolase (n: 5)	Mg-hornblende	Cannilloite	Mg-hornblende	Mg-hornblende	Mg-hornblende	Mg-hornblende	Mg-hornblende	Mg-hornblende	Actinolite (n: 15)
Location	core	core	core	core	core	core	core	core	core	rim
Oxides (wt.%)										
SiO_2	61.57	49.22	53.01	49.60	48.90	53.97	49.40	44.18	46.79	51.82
TiO_2	0.01	0.45	0.19	0.31	0.23	0.09	0.40	1.29	0.50	0.21
Al_2O_3	24.45	6.18	2.19	6.25	6.77	2.00	6.53	10.32	8.84	3.62
Cr_2O_3	-	0.00	0.61	0.00	0.05	0.034	0.02	0.06	0.04	0.13
MgO	-	11.69	13.81	11.92	11.47	18.1	13.82	9.06	10.23	13.31
CaO	5.76	12.28	18.51	12.57	12.56	12.43	12.34	12.04	12.44	12.88
MnO	0.01	0.41	0.33	0.32	0.39	0.42	0.34	0.32	0.35	0.37
FeO	0.02	16.52	10.58	15.94	15.89	14.64	16.29	17.62	17.04	15.06
Na_2O	8.41	0.66	0.28	0.49	0.61	0.29	0.63	0.94	0.71	0.38
K_2O	0.11	0.54	0.13	0.41	0.58	0.14	0.53	1.07	0.78	0.26
H_2O	-	1.90	2.08	1.98	1.99	2.06	2.08	1.96	1.93	2.01
F	-	0.27	0.02	0.12	0.07	0.19	0.00	0.03	0.14	0.09
Cl	-	0.00	0.00	0.01	0.01	0.01	0.01	0.01	0.02	0.01
Σ	100.62	100.18	101.83	99.98	99.54	104.43	102.42	98.95	99.92	100.13
nOx		23	23	23	23	23	23	23	23	
Si	2.60	7.44	7.76	7.493	7.42	7.33	7.171	6.79	7.08	7.72
Al^{TOT}	1.21									
Al^{IV}	-	0.55	0.23	0.51	0.57	0.32	0.83	1.20	0.91	0.28
Al^{VI}	-	0.52	0.11	0.57	0.52	0.00	0.20	0.61	0.53	0.28
Fe^{3+}	-	0.03	0.12	0.00	0.07	1.44	0.86	0.18	0.38	0.13
Fe^{2+}	-	1.95	1.1	1.92	1.87	0.00	1.09	2.01	1.79	1.69
Mn	-	-	-	-	-	-	-	-	-	-
Mg	-	2.49	2.83	2.51	2.53	3.56	2.83	2.07	2.29	2.85
Ca	0.26	1.95	2.00	1.96	1.99	1.66	1.88	1.98	1.98	1.94
Na	0.68	-	-	-	-	-	-	-	-	-
K	0.01	-	-	-	-	-	-	0.19	0.00	0.00
OH	-	1.01	1.956	1.02	1.03	1.85	1.95	1.03	1.03	1.64

ACCEPTED MANUSCRIPT

XMg	-	0.55	0.721	0.56	0.57	0.95	0.72	0.51	0.56	0.63
An	0.27					P1 (kbar)	1.29	5.24	3.38	
Ab	0.72					P2 (kbar)	1.08	5.51	3.43	
Or	0.01					P3 (kbar)	0.92	4.24	2.68	
						P4 (kbar)	1.92	5.65	3.9	

ACCEPTED MANUSCRIPT

ACCEPTED MANUSCRIPT

Table 5

Sample	KDH300 - 470					
Mineral	grt (n : 51)	pl (n : 10)	opx (n : 16)	amp	bt_1 (n : 17)	chl (n : 21)
Location	rim-core	core	core	core	core	core
Oxides (wt.%)						
SiO_2	38.47	63.43	51.84	43.26	35.69	25.39
TiO_2	0.05	0.02	0.05	0.10	1.84	0.04
Al_2O_3	20.42	23.88	1.306	12.75	16.13	20.73
FeO	32.77	0.13	31.12	22.17	25.19	31.52
MnO	2.60	0.03	0.92	0.30	0.13	0.34
MgO	2.41	0.00	12.12	6.31	7.94	10.82
CaO	4.44	4.64	0.53	11.21	0.16	0.05
Na_2O	0.00	9.45	0.10	1.36	0.01	0.00
K_2O	0.00	0.03	0.00	0.35	8.46	0.11
Σ	101.21	101.64	98.04	97.86	95.61	89.03
nOx	12	8	6	23	22	28
Si	3.05	2.11	2.05	6.59	5.55	5.43
Ti	0.00	0.00	0.00	0.01	0.21	0.01
Al	1.91	1.18	0.06	2.29	2.96	5.22
Fe_{tot}	2.17	0.00	1.03	2.82	3.28	5.64
Mn	0.17	0.00	0.03	0.04	0.02	0.06
Mg	0.29	0.00	0.71	1.43	1.84	3.45
Ca	0.38	0.21	0.02	1.83	0.03	0.01
Na	0.00	0.77	0.01	0.40	0.00	0.00
K	-	0.00	0.00	0.40	1.68	0.06
Σ	7.98	5.12	3.92	15.49	15.58	35.94
X_{alm}	0.72		Al^{IV}		2.44	2.56
X_{prp}	0.09		Al^{VI}		0.52	2.66
X_{grs}	0.13		X_{Fe}		0.64	0.62
X_{sps}	0.06		X_{Mg}		0.36	0.38
An		0.21				
Ab		0.78				
Or		0.01				

ACCEPTED MANUSCRIPT

Table 6

Mineral	Arsenopyrite	Arsenopyrite	Lollïngite	Pyrrhotite	Pyrrhotite	Chalcopyrite	Native gold	Electrum
Location	KDH348-139m	KDH29-318.7m	KDH348-139m	KDH300-130m	KDH29-311.8m	KDH300-130m	KDH300-394.4m	KDH29-318.7m
Host rock	Sericitized greywacke	Chloritized greywacke	Sericitized greywacke	Lithic greywacke	Biotite greywacke	Lithic greywacke	Vein	Chloritized greywacke
Spot location	core (n=6)	core (n=2)	core (n=4)	core (n=8)	core (n=2)	core (n=7)	core (n=4)	core (n=15)
Oxides (wt.%)								
S	18.55	17.00	2.95	38.74	38.59	35.05	0.0525	0.46
Fe	33.68	28.14	27.37	58.89	58.25	29.38	0.2	1.02
Co	0.08	4.96	0.09	0.05	0.10	0.01	0.015	0.16
Ni	0.12	0.41	0.82	0.02	0.22	0.01	0	0.01
Cu	0	0	0.01	0.01	0	34.47	0.01	0.01
Zn	0	0	0	0		0	0	0
As	48.74	50.55	69.82	0.03	0.01	0.02	0	1.08
Ag	0	0	0	0	0	0.01	2.81	9.74
Sb	0	0	0	0	0	0	0	0
Te	0	0	0	0	0	0	0	0
Au	0	0	0.02	0	0	0	92.62	87.67
Pb	0.06	0.09	0.04	0.10	0.09	0.06	0	0
Bi	0.1	0.14	0.05	0.06	0.03	0.04	0.28	0.41
Total	101.33	101.31	101.16	97.93	97.36	99.07	96.01	100.59
At.% As	35.44	36.45						
Ni/Co	1.5	0.08	9.11	0.44	2.14	1	0	0.04
Apy thermometer (T en°C) (Sharp et al., 1985)	360	475						

ACCEPTED MANUSCRIPT

Table 3

Sample	KDH291-56.2				KDH29-311.8								KDH300-394.5	
Number	c1-2	c1-4	c1-8	c1-10	6	9	14	19	4	17	8	10	c6.1	c3.1
Mineral	Bt2	Bt2	Bt2	Bt2	Bt1	Bt1	Bt1	Bt1	Bt2	Bt2	Bt2	Bt2	Bt1	Bt3
Location	Matrix	Matrix	Matrix	Matrix	Matrix	Matrix	Matrix	Matrix	Matrix	Matrix	Matrix	Matrix	Matrix	Vein
Oxides (wt.%)														
SiO_2	36.93	37.03	34.86	36.39	36.54	35.10	35.09	35.77	35.67	35.29	34.84	35.70	34.31	37.41
TiO_2	1.10	1.35	0.88	1.13	1.36	1.28	1.45	1.51	1.38	1.33	1.36	1.68	2.40	0.93
Al_2O_3	17.98	17.51	17.83	17.69	18.00	19.28	18.71	18.19	18.65	18.34	18.72	17.89	17.67	17.59
FeO	16.42	15.39	17.63	16.62	16.57	16.98	17.00	17.18	16.60	18.31	16.37	15.82	22.55	12.72
MnO	0.17	0.18	0.26	0.19	0.19	0.31	0.27	0.17	0.32	0.28	0.23	0.18	0.43	0.93
MgO	13.60	13.70	14.42	13.66	13.01	12.18	12.06	12.20	12.05	12.19	12.50	12.52	7.46	15.85
CaO	0.04	1.83	0.02	0.09	0.00	0.02	0.00	0.01	0.00	0.00	0.03	0.04	0.00	0.00
Na_2O	0.09	0.10	0.06	0.09	0.06	0.08	0.13	0.17	0.10	0.06	0.14	0.08	0.00	0.00
K_2O	9.38	8.88	7.34	9.07	8.97	8.59	8.82	8.99	8.70	8.58	9.18	8.76	10.03	9.67
Σ	95.71	95.97	93.30	94.93	94.69	93.82	93.54	94.19	93.48	94.36	93.36	92.66	93.97	95.14
nOx	22	22	22	22	22	22	22	22	22	22	22	22	22	22
Si	5.51	5.50	5.33	5.48	5.50	5.34	5.375	5.443	5.444	5.382	5.346	5.480	5.51	5.36
Al^{IV}	2.49	2.50	2.67	2.52	2.49	2.65	2.625	2.557	2.556	2.618	2.654	2.520	2.10	2.45
Al^{VI}	0.67	0.56	0.55	0.62	0.69	0.81	0.754	0.706	0.799	0.679	0.733	0.718	1.14	0.59
Ti	0.12	0.15	0.10	0.13	0.15	0.14	0.167	0.173	0.158	0.153	0.157	0.194	0.28	0.10
Fe	2.05	1.91	2.26	2.09	2.08	2.16	2.178	2.186	2.119	2.335	2.101	2.031	2.95	1.58
Mn	0.02	0.02	0.03	0.02	0.02	0.04	0.035	0.022	0.041	0.036	0.030	0.023	0.05	0.10
Mg	3.02	3.03	3.29	3.07	2.92	2.765	2.753	2.767	2.741	2.770	2.859	2.864	1.74	3.48
Ca	0.01	0.29	0.00	0.01	0.00	0.003	0.000	0.002	0.000	0.000	0.005	0.007	0.00	0.00
Na	0.03	0.03	0.02	0.03	0.02	0.024	0.039	0.050	0.030	0.018	0.042	0.024	0.00	0.00
K	1.78	1.68	1.43	1.74	1.72	1.670	1.724	1.745	1.694	1.669	1.797	1.716	2.00	1.81
X_{Mg}	0.60	0.61	0.59	0.59	0.58	0.56	0.56	0.56	0.56	0.54	0.58	0.59	0.37	0.69

ACCEPTED MANUSCRIPT

ACCEPTED MANUSCRIPT

Table 7

Sample	KDH29-56.2				KDH 311.8		
Analyses	c1.17	c2.3	c3.12	c3.24	c1.1	c1.2	c1.5
Mineral	tur2	tur2	tur2	tur2	tur2	tur2	tur2
Location	core	core	core	core	core	core	core
Oxides (wt%)							
SiO_2	35.88	36.00	35.24	35.7	36.15	36.01	35.73
Al_2O_3	31.16	30.54	31.81	32.48	34.69	32.03	33.89
TiO_2	0.99	1.09	0.31	0.17	0.21	0.78	0.34
FeO(T)	5.04	5.6	4.79	5.13	4.63	5.52	4.9
MgO	9.31	9.31	8.84	8.48	7.58	8.47	7.74
CaO	1.63	1.48	0.83	0.53	1.22	1.65	1.24
Na_2O	1.96	1.91	2.16	2.08	1.59	1.5	1.57
LiO_2*	0.129	0.111	0.09	0.099	0.18	0.02	0.15
B_2O_3*	10.311	10.446	10.074	10.259	10.49	10.41	10.23
H_2O*	3.18	3.315	3.221	3.278	3.17	3.16	3.1
Σ	95.62	97.872	93.386	95.636	96.84	96.58	94.47
nOx	24.5	24.5	24.5	24.5	24.5	24.5	24.5
Si^T	6.06	5.99	6.04	5.93	5.96	6.01	5.95
Al^T	0.00	0.01	0.00	0.07	0.04	0.00	0.05
T Total	6.068	6.00	6.038	6.00	6.00	6.01	6.00
Al^Z	5.96	5.873	6.00	6.00	6.00	6.00	6.00
Mg^Z	0.04	0.127	0.00	0.00	0.00	0.00	0.00
Fe^{3+Z}	0.00	0.00	0.00	0.00	0.00	0.00	0.00
Z total	6.00	6.00	6.00	6.00	6.00	6.00	6.00
Al^Y	0.00	0.00	0.303	0.319	0.6	0.3	0.56
Ti^Y	0.127	0.125	0.00	0.00	0.00	0.00	0.00
Fe^{2+Y}	0.564	0.696	0.577	0.708	0.55	0.7	0.57

ACCEPTED MANUSCRIPT

Table 8

Spot	Element concentrations (ppm)			Element Ratio	Radiogenic ratios							Ages (in Ma)						
	Pb	U	Th	Th/U	$^{207}Pb/^{235}U$	±	$^{206}Pb/^{238}U$	±	Rho[a]	$^{207}Pb/^{206}Pb$	±	$^{207}Pb/^{206}Pb$	±	$^{206}Pb/^{238}U$	±	$^{207}Pb/^{235}U$	±	%conc[b]
1	256	537	447	0.83	7.1871	0.0870	0.3879	0.0046	0.98	0.1344	0.0014	2156	18	2113	21	2135	11	99.0
2	196	527	170	0.32	6.2539	0.0757	0.3452	0.0041	0.98	0.1314	0.0014	2117	18	1912	20	2012	11	95.0
3	118	245	228	0.93	7.1888	0.0873	0.3917	0.0046	0.97	0.1331	0.0014	2140	18	2131	21	2135	11	99.8
4	190	398	367	0.92	7.1747	0.0871	0.3866	0.0046	0.97	0.1346	0.0014	2159	18	2107	21	2133	11	99.0
5	275	575	669	1.16	6.8155	0.0830	0.3717	0.0044	0.97	0.1330	0.0014	2138	18	2038	21	2088	11	97.7
6	207	502	181	0.36	6.9958	0.0853	0.3802	0.0045	0.97	0.1335	0.0014	2144	18	2077	21	2111	11	98.5
7	106	227	173	0.76	7.2281	0.0889	0.3910	0.0046	0.96	0.1341	0.0014	2152	18	2127	22	2140	11	99.4
8	198	418	445	1.06	6.8509	0.0845	0.3772	0.0045	0.97	0.1317	0.0014	2121	18	2063	21	2092	11	98.6
9	261	548	403	0.74	7.1623	0.0884	0.3933	0.0047	0.96	0.1321	0.0014	2126	18	2138	22	2132	11	100.3
10	249	514	577	1.12	7.0208	0.0868	0.3813	0.0045	0.96	0.1336	0.0014	2145	18	2082	21	2114	11	98.6
11	190	421	253	0.6	7.2622	0.0901	0.3926	0.0047	0.96	0.1342	0.0014	2153	19	2135	22	2144	11	99.6
12	174	393	253	0.64	7.0616	0.0878	0.3860	0.0046	0.96	0.1327	0.0014	2134	19	2104	21	2119	11	99.3
13	178	371	355	0.96	7.1479	0.0892	0.3890	0.0046	0.96	0.1333	0.0014	2142	19	2118	22	2130	11	99.4
14	197	398	430	1.08	7.2038	0.0900	0.3913	0.0047	0.96	0.1335	0.0014	2145	19	2129	22	2137	11	99.6
15	200	467	207	0.44	7.1787	0.0905	0.3927	0.0047	0.95	0.1326	0.0014	2133	19	2135	22	2134	11	100.1
16	212	420	519	1.24	7.1801	0.0908	0.3927	0.0047	0.95	0.1326	0.0015	2133	19	2135	22	2134	11	100.0
17	197	422	334	0.79	2.2262	0.0915	0.3921	0.0047	0.95	0.1337	0.0015	2147	19	2133	22	2140	11	99.7
18	334	823	98	0.12	7.0293	0.0891	0.3797	0.0046	0.95	0.1343	0.0015	2155	19	2075	21	2115	11	98.2
19	217	425	538	1.27	7.1652	0.0912	0.3917	0.0047	0.94	0.1327	0.0015	2134	19	2131	22	2132	11	99.9
20	189	382	422	1.1	7.2337	0.0924	0.3923	0.0047	0.94	0.1338	0.0015	2148	19	2133	22	2141	11	99.7
21	258	574	535	0.93	6.6133	0.0846	0.3643	0.0044	0.94	0.1317	0.0015	2120	19	2003	21	2061	11	97.2
22	135	291	246	0.85	7.1474	0.0921	0.3897	0.0047	0.93	0.1330	0.0015	2138	19	2122	22	2130	11	99.6

[a] rho: error correlation of $^{207}Pb/^{235}U$ and $^{206}Pb/^{238}U$ defined as ($err^{206}Pb/^{238}U\%$)/($err^{207}Pb/^{235}U\%$)

[b] Concordance calculated as ($^{207}Pb/^{235}U/^{207}Pb/^{206}Pb$)*100

Errors are listed at 1σ

ACCEPTED MANUSCRIPT

ACCEPTED MANUSCRIPT

Table 9

Samples	Minerals	Sample mass (g)	[Re] (ppb) [1]	^{187}Re (ppb) [1,2,3] ± 2σ	Total ^{188}Os (ppt) [4]	% ^{188}Os from blank	Total ^{187}Os (ppt)	% ^{187}Os * [5]	^{187}Os * (ppt) [2,5]	^{187}Os*/^{187}Re [1,2,5] ± 2σ	Age (Ma) [2,6] ± 2σ	MSWD	^{187}Re/^{188}Os	^{187}Os/^{188}Os	rho
KDH280-101b	Po	0.30387	2.33	1.46 ± 0.01	1.51	10	54.1	98.6	53.34 ± 0.62	0.0365 ± 0.0007	2151 ± 43		1080 ± 123	40 ± 5	0.9896
KDH280-101c	Po	0.30696	2.48	1.56 ± 0.01	1.51	9	58.1	98.7	57.39 ± 0.63	0.0368 ± 0.0007	2168 ± 40		1144 ± 130	43 ± 5	0.9907
KDH280-101d	Po	0.30047	2.37	1.49 ± 0.01	1.50	10	55.1	98.6	54.37 ± 0.63	0.0365 ± 0.0007	2150 ± 42		1104 ± 126	41 ± 5	0.9897
										sample/deposit weighted mean	**2157 ± 24**	**0.25**			

[1] Re data are blank corrected.

[2] All listed uncertainties are 2σ.

[3] Uncertainty on ^{187}Re includes measurement precision, blank uncertainty, weighing errors and uncertainty on spikes calibration.

[4] Includes both common osmium contained in the sample and the contribution from the blank.

[5] ^{187}Os* = ^{187}Os radiogenic only, calculated assuming a natural osmium ratio of ^{187}Os/^{188}Os = 0.5 ± 0.4. Uncertainty on ^{187}Os* includes the uncertainty on this ratio, measurement precision, weighing errors, uncertainty on spikes calibration and uncertainty on standard measurements.

[6] Assuming λ^{187}Re = 1.666 x 10^{-11} yr^{-1} (Smoliar et al., 1996).

ACCEPTED MANUSCRIPT

ACCEPTED MANUSCRIPT

Figure captions

Figure 1: Geology of West African craton (modified after Castaing et al., 2003; Naba et al., 2003, Milesi et al., 2004, Vegas et al., 2008, Ganne et al., 2011). The Kénéma Man domain (Archean nucleus) and the Baoule-Mossi domain (Paleoproterozoic juvenile crust) form two distinct domains separated by the Sassandra Fault (SF). Volcano-sedimentary belts include Banfora (BA), Houndé (HO), Boromo (BO), Lawra (LW), Goren (GO), Bui (BU), Ashanti (AS) and Sefwi (SW), Haute Comoé basin (HC) and Manga Fada-N'Gourma belt (MFG). These belts are separated into dark green for mafic volcanics rocks and light green for volcano-sedimentary rocks and intermediate to felsic igneous rocks (Baratoux et al., 2011). A spatial association between gold deposits of the Baoulé-Mossi and major structures such as the Grenville-Ferkessedougou-Bobo-Dialousso (GFBF), Ouango-Fitini (OF) and Markoye (MSZ; this study) shear zones is observed in the Baoulé-Mossi domain.

Figure 2: Geology of the Manga-Fada-N'Gourma area with MSZ (thick black lines) and location of the Kiaka gold deposit (compiled after Hottin et Ouédrago, 1975; Milési et al., 1992; Castaing et al., 2003; Naba et al., 2004 and Vegas et al., 2007).

Figure 3: Local geology of the Kiaka deposit and drillhole and cross-section locations. The KDH300 drillhole was sampled for geochronology, petrographic study and P-T estimation. Mineralized envelopes are projected at surface from drillhole data.

Figure 4: NW-trending cross-sections (A: 6100, B: 5800), plan view and longitudinal section within the Kiaka deposit. The 6100 section illustrates the relationship between the porphyric diorite, metagreywacke rocks and gold mineralization and the 5800 show structural and

ACCEPTED MANUSCRIPT

lithological control on ore bodies. Plan and longitudinal sections illustrates the contour of inferred pit and the associated gold distribution with potential ore shoots.

Figure. 5: Macroscopic examples of key samples from the Kiaka host rocks. Quartz-muscovite greywacke (A) and lithic greywacke (B) and Aluminosilicate-bearing metapelites (C). The porphyric diorite intrusion (D; KDH337-44.1) is also found at the vicinity of ore shoots. Most of contact between quartz-biotite metagreywacke and metavolcanic rock are strongly altered and deformed but some are locally preserved (E).

Figure 6: Photomicrographs under transmitted light (a, c and d) or crossed polarized light (b) and metamorphic paragenesis with various inferred protoliths. Petrography of less altered host rocks including volcano-sedimentary units (a, b, c) and diorite intrusion (d) associated with the Kiaka gold deposit. Aluminosilicate-bearing metagreywacke (KDH348- 44.5) are located in south footwall of D_2-related shear zones and are locally mineralized (See Fig. 11d for details). A garnet-orthopyroxene-bearing volcano-sedimentary unit (c, KDH300-470) is used to estimate M2 metamorphic peak (for details, see Table 4) probably associated with diorite emplacement (d).

Figure 7: Total alkalis vs. SiO_2 diagram (A) from Cox et al., 1979, spider diagram (B; primitive mantle normalizing values from McDonough and Sun, 1995) and selected REE plot (C; chondritic normalizing values from Sun and McDonough, 1995) for the diorite KDH337-44.1 (Fig. 5F and Fig. 8d and 11f) showing similarities with the Tenkodogo-Yamba batholith samples T15 and DD17 (Naba et al., 2014), the sample FC97 (described as tonalitic basement) of Vegas et al., 2008 and the Morila diorites MANU-125 and MANU-126 (McFarlane et al., 2011).

ACCEPTED MANUSCRIPT

Figure 8: Photomicrographs of outcrops (A, B, D) and drill core sample (C, E and G). PK_1 folds (A) are more open that isoclinal PK_2 folds (C and G) and appears as relicts preserved from the transposition during D_2 deformation. Specially, those FK_1 folds are observed in metapelites but not in mafic rocks (C). Note that pyrrhotite aggregates (red) are affected by SK_2 foliation (E) and aluminosilicate porphyroblasts (grey) are muscovite-rich and kyanite is also found as relicts. SK_2 shear bands are also observed (D; right side panels are sketches of photographs shown on left side) and are associated LK_2 mineral lineation (B). Example of aluminosilicate-bearing metapelites show (F) evidence of reverse movement along SK_2 shear bands (outcrop location: long. 739288; lat. 1289019; UTM WGS84), and folding (G)

Figure 9: Stereoplot showing the main planar and linear structures within the Kiaka deposit inglucind poles of SK_2 metamorphic foliation (green circles), LK_2 mineral lineation (brown triangles), $DK_{3\text{-}4}$ vein planes (dark and red squares) and FK_1 fold axis (blue squares).

Figure 10: Paragenetic sequence of the Kiaka gold deposit with emphasis on the relationships between mineralization styles (disseminated and vein stages) and hydrothermal assemblages.

Figure 11: Examples of the superposition of hydrothermal alteration within metasedimentary rocks. Photomicrographs of the typical ore style of the disseminated stage composed of a deformed biotite-clinozoïzite-pyrrhotite-pyrite-chalcopyrite assemblage hosted by the lithic metagreywacke (A; KDH280-101m; Re-Os sample). DK_3 Hydrothermal breccia in metapelites associated with silicification and actinolite and diopside alteration (B), DK_3 diopside veins associated with epidote-actinolite alteration cuts by DK_4 carbonate veinlets (C). Chlorite-carbonate alteration assemblage with visible gold and electrum in the chlorite sheets

ACCEPTED MANUSCRIPT

ore within fracturated clinozoïzite (See Fig. 12 for details) overprinting a biotite-clinozoïzite alteration stage (D; KDH29-318.7m). Calcite vein associated with chloritization (Chl_2) cuts a mineralized biotite tourmaline assemblage (E; KDH291-56.2m). Pyrrhotite, chalcopyrite and pyrite are the main sulfides present while biotite aggregates are intergrown with clinozoïsites and titanite. Tourmaline contains sulfides, chlorite (Chl_1) and amphibole as inclusions. Sulfides (pyrrhotite and chalcopyrite) are indicated in red (E).

Figure 12: Microphotographs under natural light of pyrrhotite-pyrite-chalcopyrite assemblage in aluminosilicate-bearing pelites (A, KDH348-44.5). Reflected light images of quartz-biotite metagreywacke (B, KDH300-130). Arsenopyrite and lollïngite appears to be replaced by pyrrhotite in metapelites (C, KDH348-139). Visible gold is locally found in quartz-carbonates veins within quartz muscovite schist (D, same sample as Fig. 11D). SEM/BSE images of electrum is sometimes associated with arsenopyrite with Co zonation (E) and pyrrhotite found in association with electrum, chalcopyrite and contains inclusions of bismuth telluride (F).

Figure 13: Photomicrographs under natural light (A, B, C and E) or crossed polarized light (D and F). Petrography of hydrothermally altered host rocks including volcano-sedimentary units (A, B, C, D and E) and diorite intrusion (F) associated with the Kiaka gold deposit. Biotitization locally associated with disseminated tourmaline and clinozoïzite. Actinolite developed in corona textures around Mg-hornblende (F).

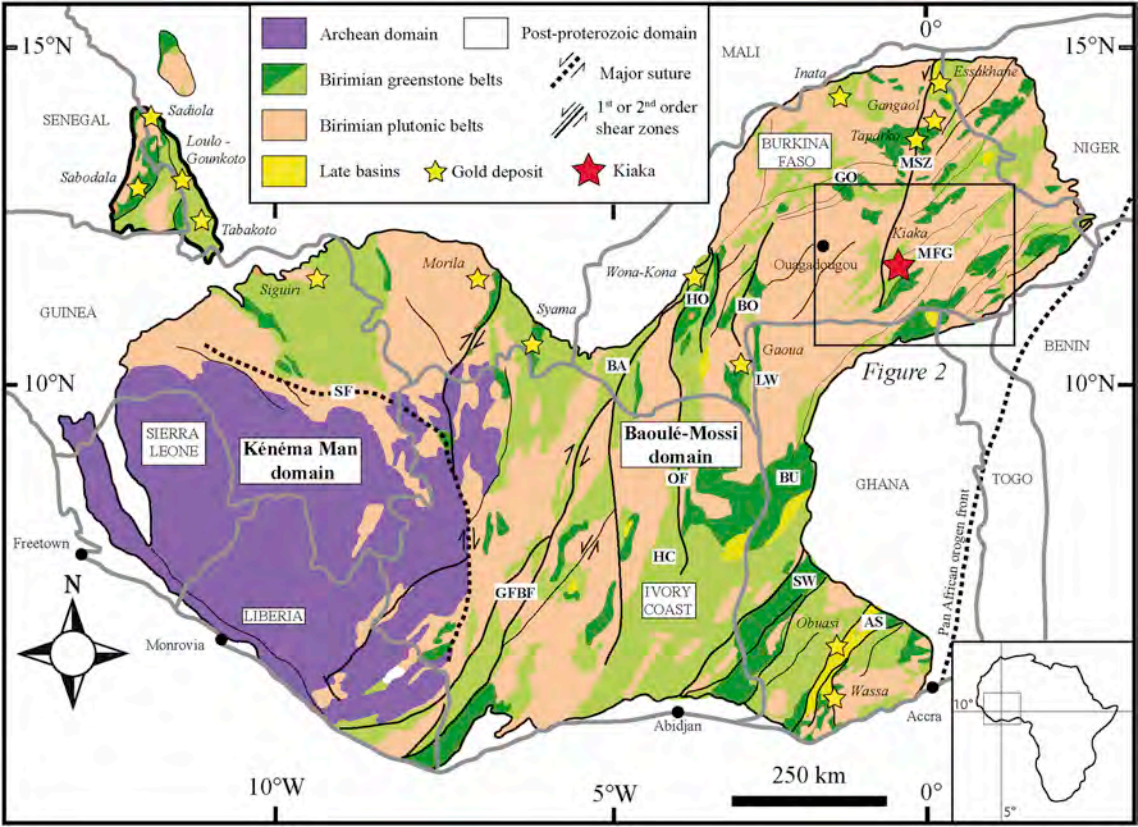
Figure 14: Zircon U-Pb Concordia plot of the sample KDH337 – 105.5 m with examples of subeuhedral zircons within the diorite. See Table 8 for details. TL, transmitted light; CL, cathodoluminescence.

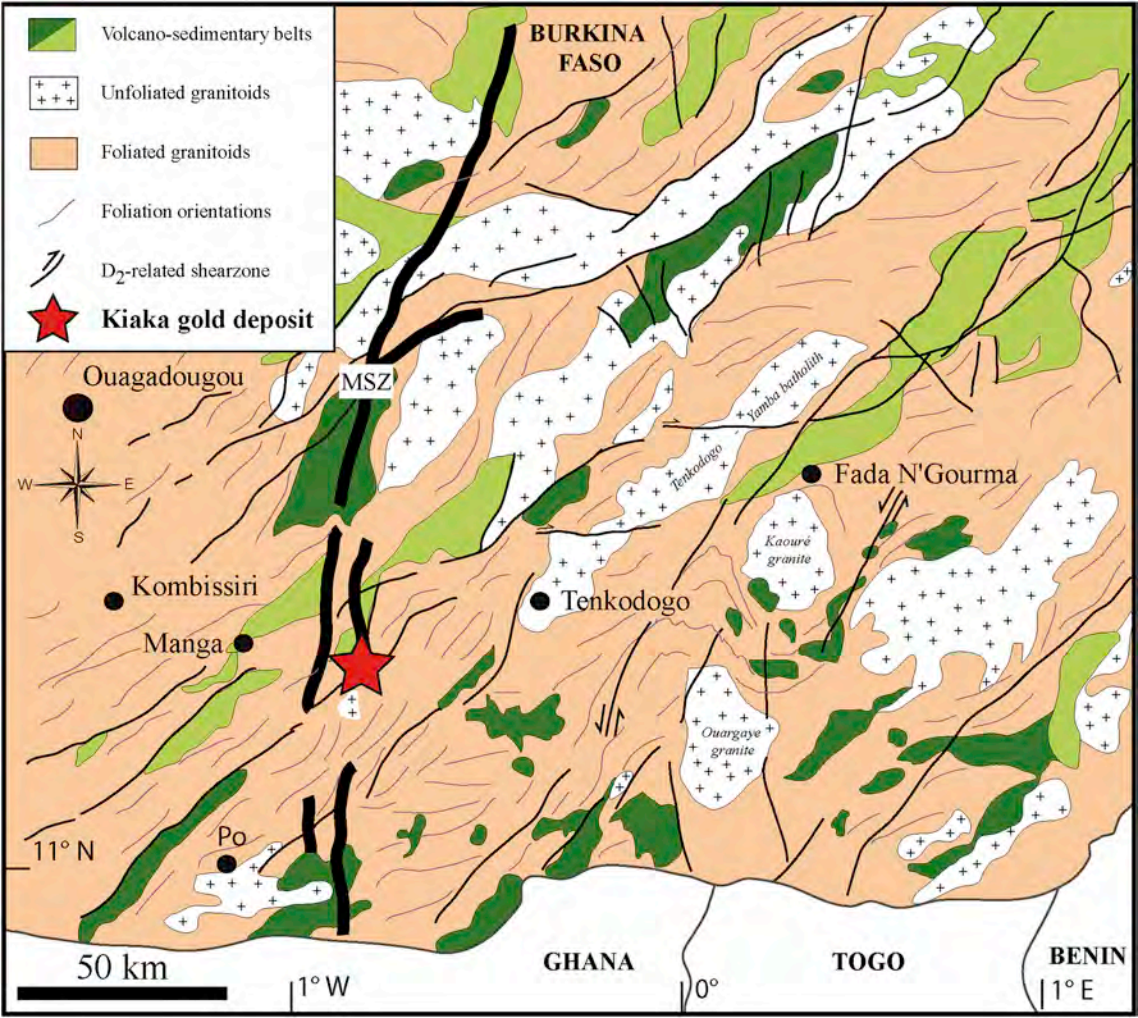
ACCEPTED MANUSCRIPT

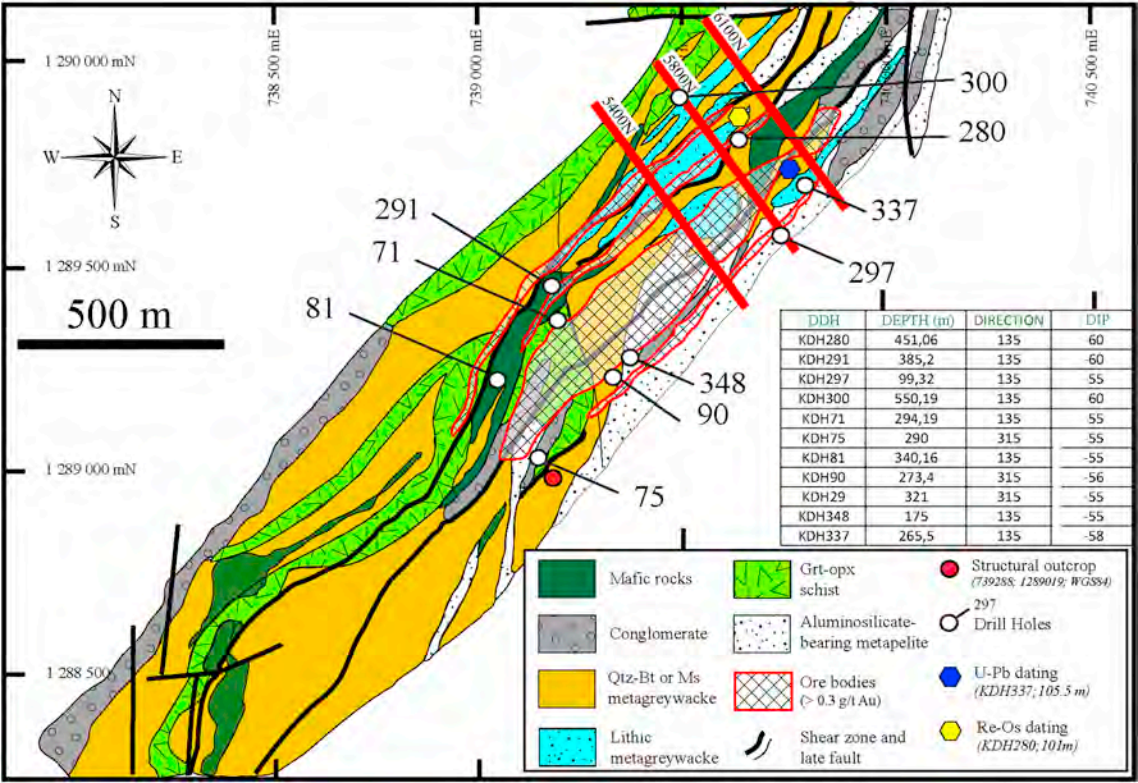
Figure 15: Idealized 3D diagram representing key geological features and P-T diagram with peak metamorphism estimate for the Kiaka area and some recent metamorphic data of the Baoulé-Mossi domain from Ganne et al., 2011 (Manga-Fada-N'Gourma belt), and Block et al., 2015 (northern Ghana).

Figure 16: Compilation of the geochronological data for plutonic (light gray symbols) and volcanic (dark gray symbols) magmatic rocks and gold mineralizing events within the Baoulé-Mossi domain placed within the framework of the tectono-metamorphic evolution and magmatic activity of the region. Dark and light gray lines refer to age uncertainties. Age references: (1) Agyei Duodu et al., 2009; (2) Baratoux and Brugier, 2013, unpublished data; (3) Brugier et al., 2013, unpublished data; (4) Castaing et al., 2003; (5) Ennih and Liégeois, 2008; (6) Klockner, 1991; (7) Le Métour et al., 2003; (8) Lompo, 1991; (9) McCuaig et al., 2014, unpublished data ; (10) Ama Salah et al., 1996; (11) Schwartz, 2003; (12) Simeon et al., 1992; (13) Siegfried et al., 2009; (14) Tapsoba et al., 2013; (15) Thomas et al., 2009; (16) Block et al., 2015; (17) Miller et al., 2014, unpublished data; (18) Le Mignot et al. 2016b and (*) this study. Geod., Meta. And Def., respectively, refers to Geodynamic, Metamorphism and Deformation.

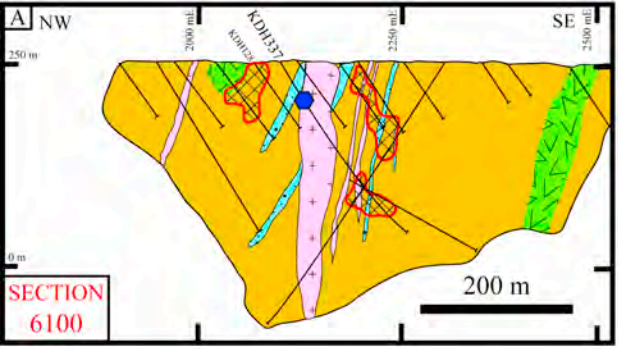
ACCEPTED MANUSCRIPT

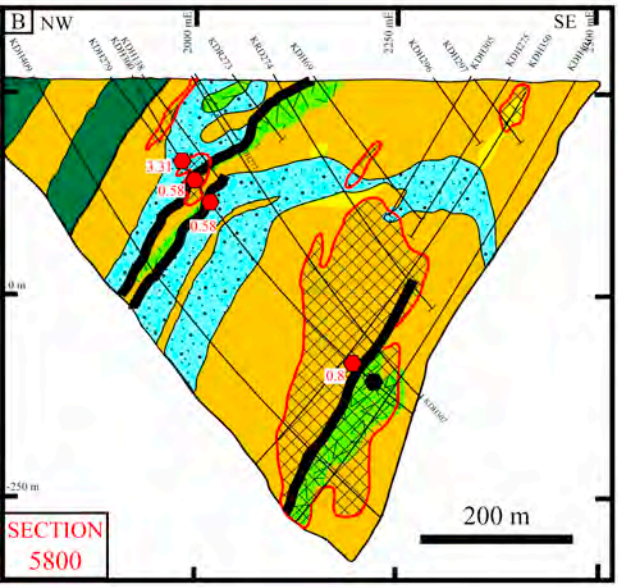

Archean domain
Birimian greenstone belts
Birimian plutonic belts
Late basins
Post-proterozoic domain
Major suture
1st or 2nd order shear zones
Gold deposit
Kiaka
15°N
0°
MALI
Inata
Essakhane
Gangaol
Tapoko
BURKINA FASO
MSZ
GO
NIGER
Kiaka
MFG
Ouagadougou
SENEGAL
Sadiola
Loulo - Gounkoto
Sabodala
Tabakoto
Morila
Siguiri
Wona-Kona
HO
BO
Syama
GUINEA
BA
Gaoua
LW
BENIN
Figure 2
10°N
SF
SIERRA LEONE
Kénéma Man domain
Baoulé-Mossi domain
OF
BU
GHANA
TOGO
Pan African orogen front
Freetown
HC
SW
N
GFBF
IVORY COAST
Obuasi
AS
LIBERIA
Monrovia
Wassa
Abidjan
Accra
10°W
5°W
250 km
10°
5°

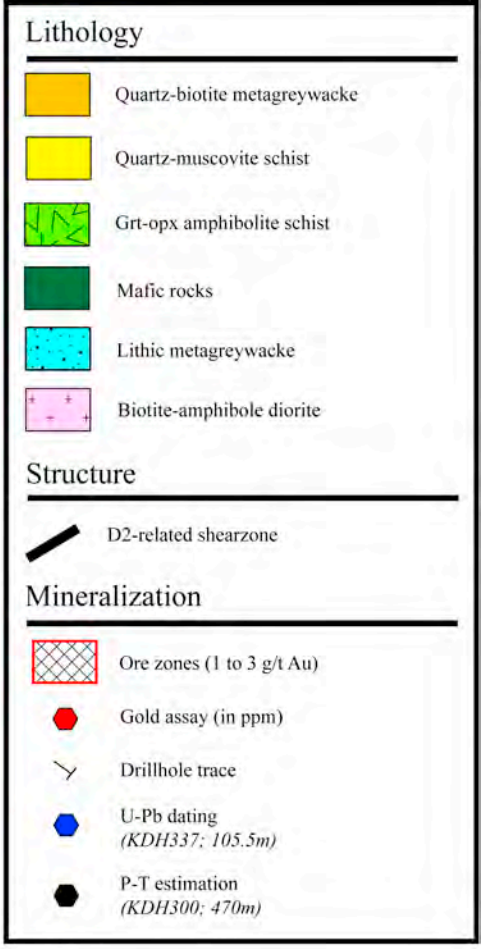

Volcano-sedimentary belts
Unfoliated granitoids
Foliated granitoids
Foliation orientations
D2-related shearzone
Kiaka gold deposit
BURKINA FASO
Ouagadougou
MSZ
N
W
E
S
Yamba batholith
Tenkodogo
Fada N'Gourma
Kaouré granite
Kombissiri
Tenkodogo
Manga
Ouargaye granite
11° N
Po
50 km
GHANA
TOGO
BENIN
1° W
0°
1° E

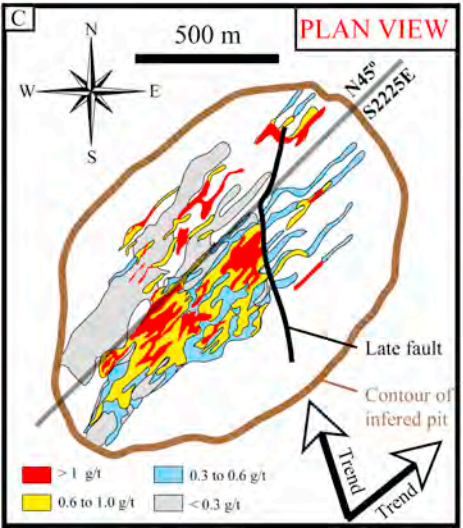


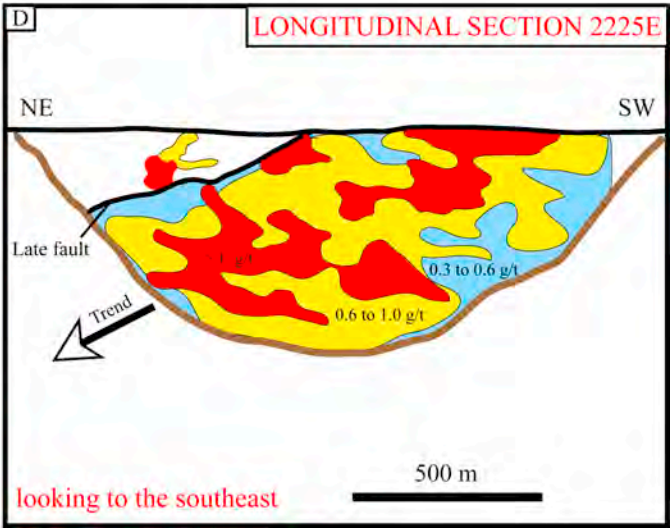
DDH	DEPTH (m)	DIRECTION	DIP
KDH280	451,06	135	60
KDH291	385,2	135	-60
KDH297	99,32	135	55
KDH300	550,19	135	60
KDH71	294,19	135	55
KDH75	290	315	55
KDH81	340,16	135	-55
KDH90	273,4	315	-56
KDH29	321	315	-55
KDH348	175	135	-55
KDH337	265,5	135	-58

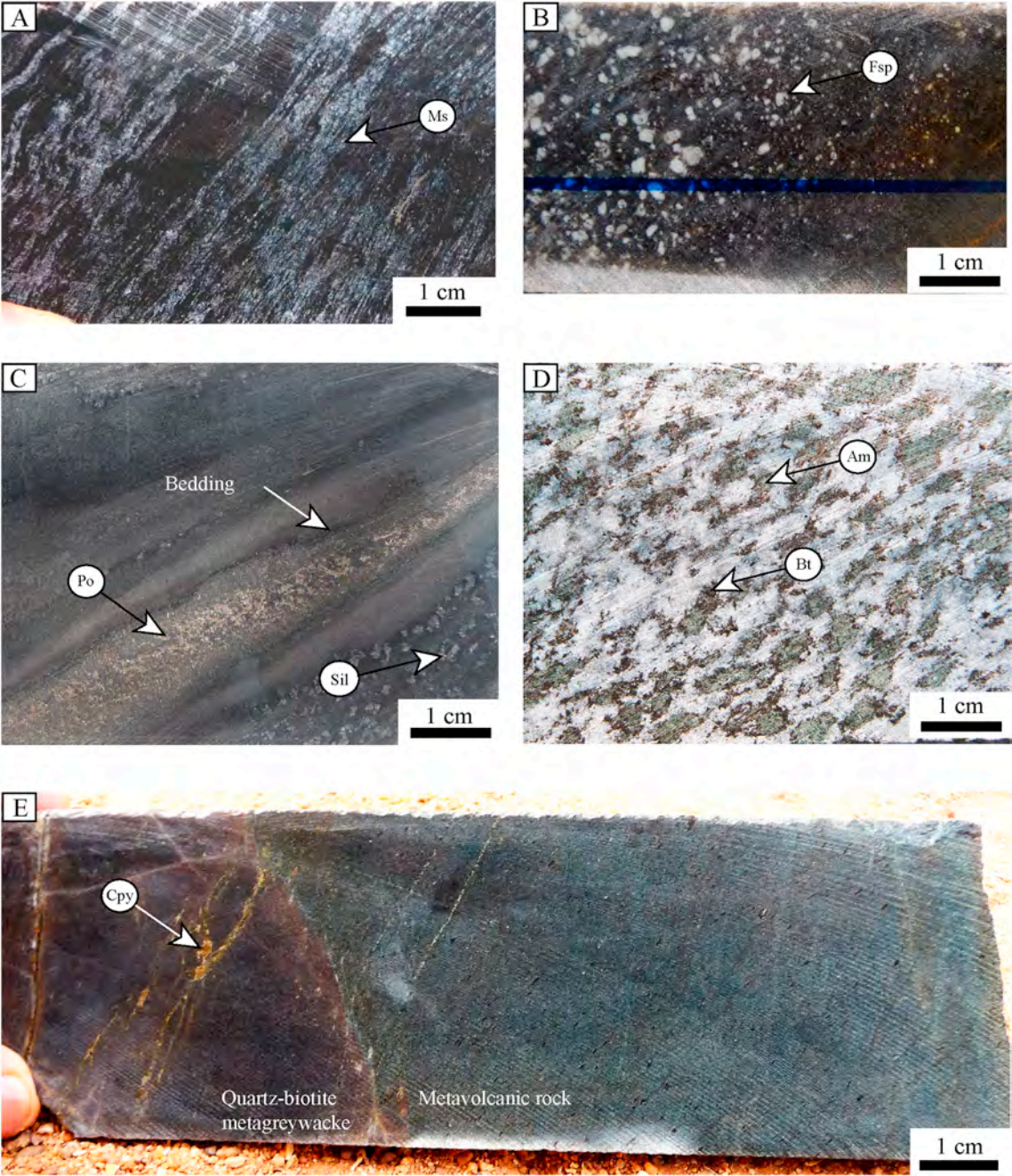

A
NW
SE
2000 mE
2250 mE
2500 mE
KDH337
250 m
0 m
SECTION
6100
200 m

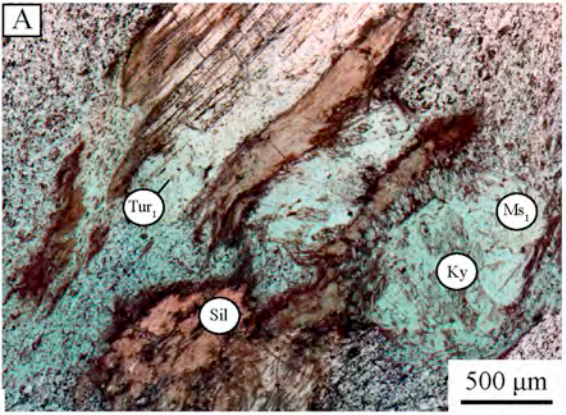

B
NW
SE
2000 mE
2250 mE
2500 mE
KDH409
KDH279
KDH318
KDH268
KDH273
KDH274
KDH269
KDH296
KDH295
KDH305
KDH275
KDH350
KDH406
3.31
0.58
1.58
0.8
KDH307
0 m
-250 m
SECTION
5800
200 m

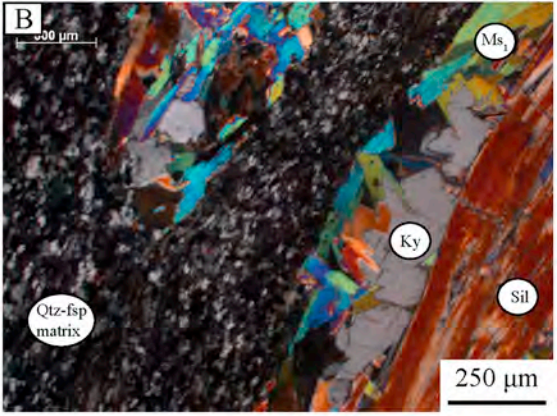

Lithology
Quartz-biotite metagreywacke
Quartz-muscovite schist
Grt-opx amphibolite schist
Mafic rocks
Lithic metagreywacke
Biotite-amphibole diorite
Structure
D2-related shearzone
Mineralization
Ore zones (1 to 3 g/t Au)
Gold assay (in ppm)
Drillhole trace
U-Pb dating
(KDH337; 105.5m)
P-T estimation
(KDH300; 470m)

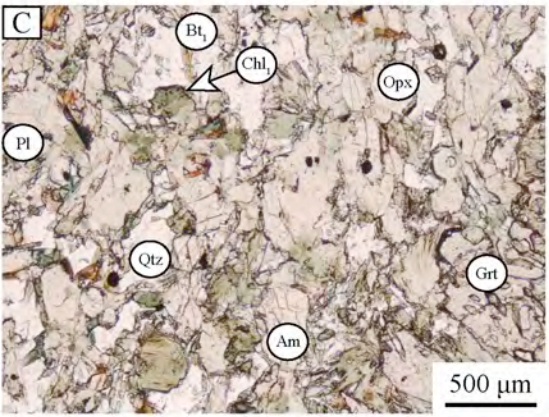

C
PLAN VIEW
N
W
E
S
500 m
N45°
S2225E
Late fault
Contour of
infered pit
Trend
Trend
> 1 g/t
0.3 to 0.6 g/t
0.6 to 1.0 g/t
< 0.3 g/t

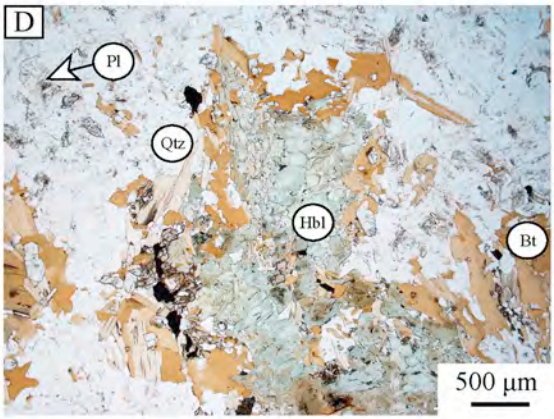

D
LONGITUDINAL SECTION 2225E
NE
SW
Late fault
> 1 g/t
0.3 to 0.6 g/t
0.6 to 1.0 g/t
Trend
looking to the southeast
500 m


A
Ms
1 cm
B
Fsp
1 cm
C
Bedding
Po
Sil
1 cm
D
Am
Bt
1 cm
E
Cpy
Quartz-biotite
metagreywacke
Metavolcanic rock
1 cm



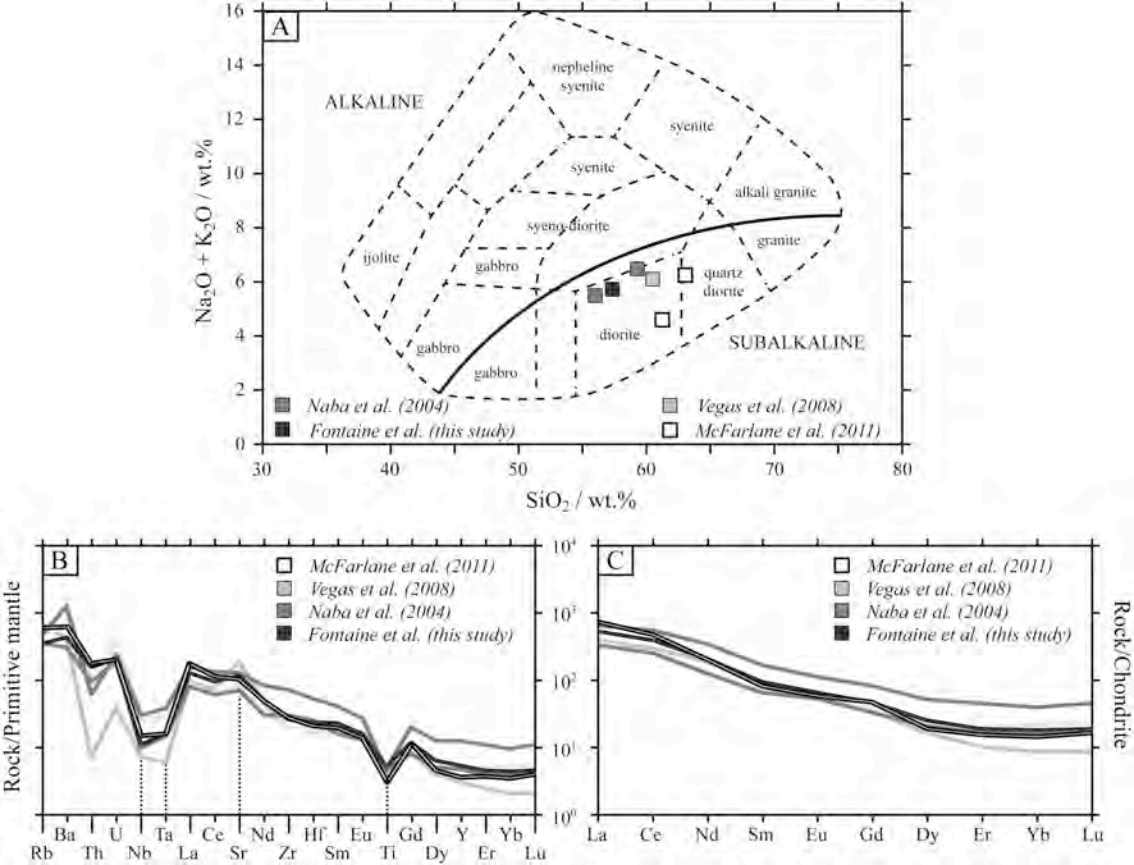


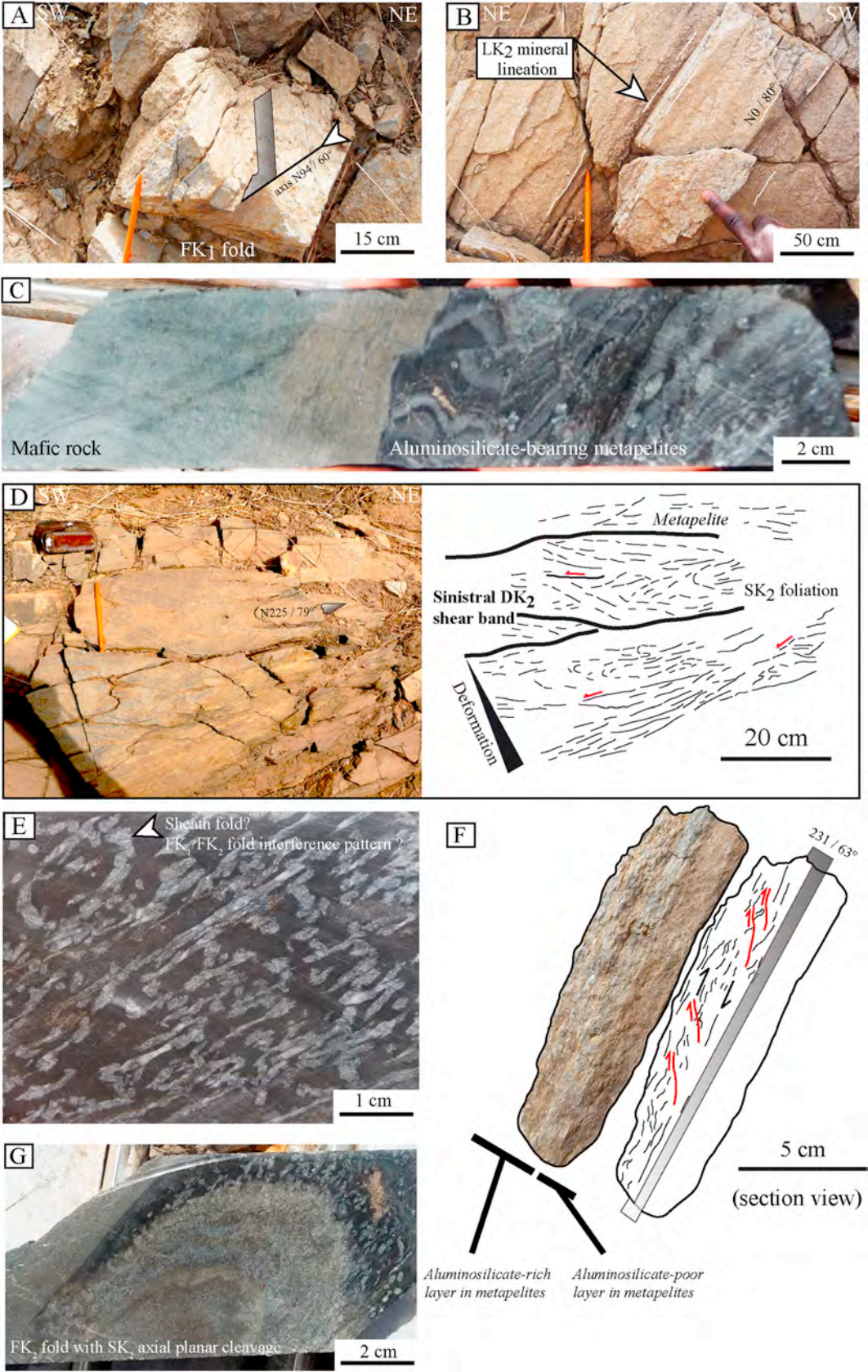


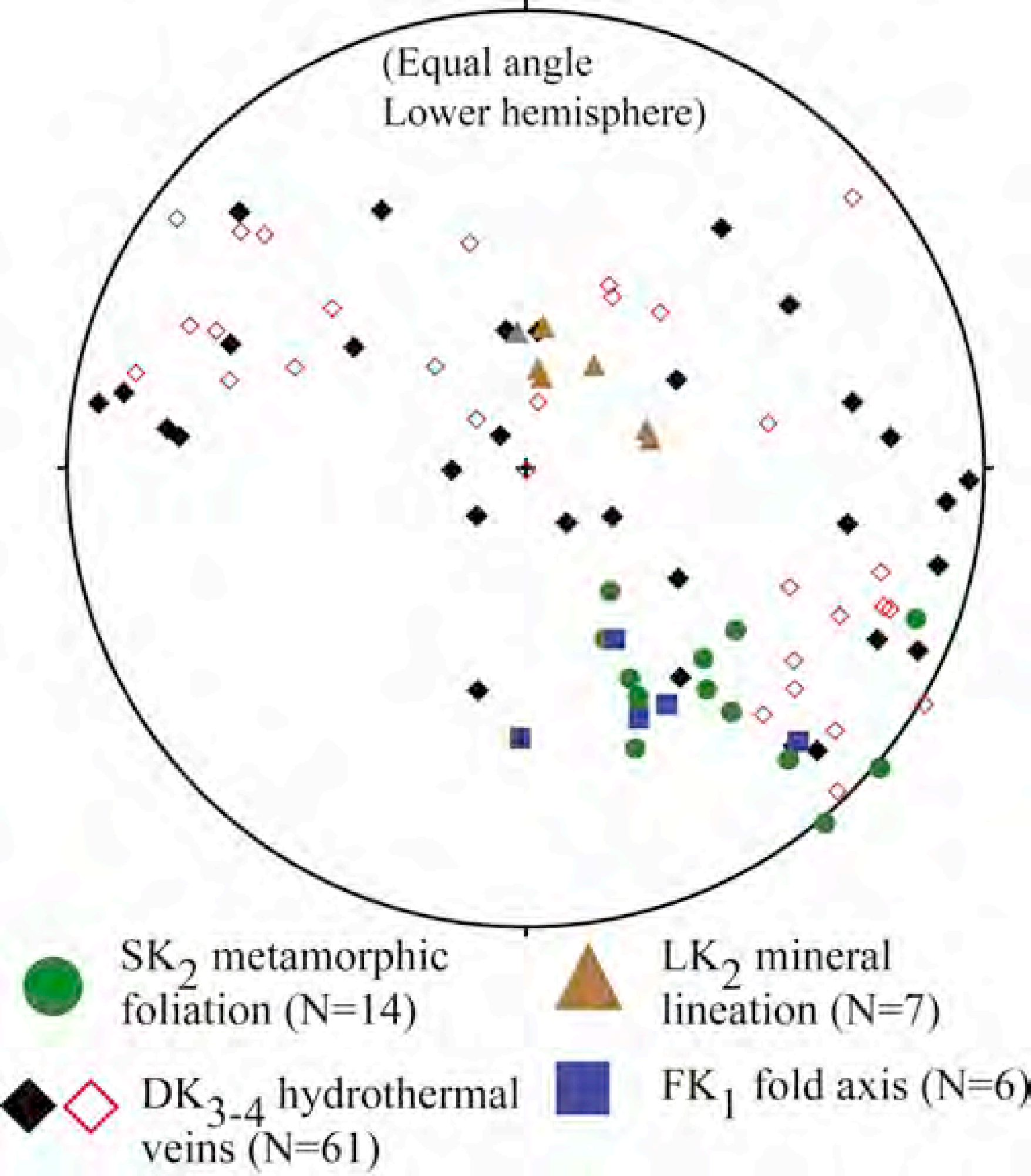


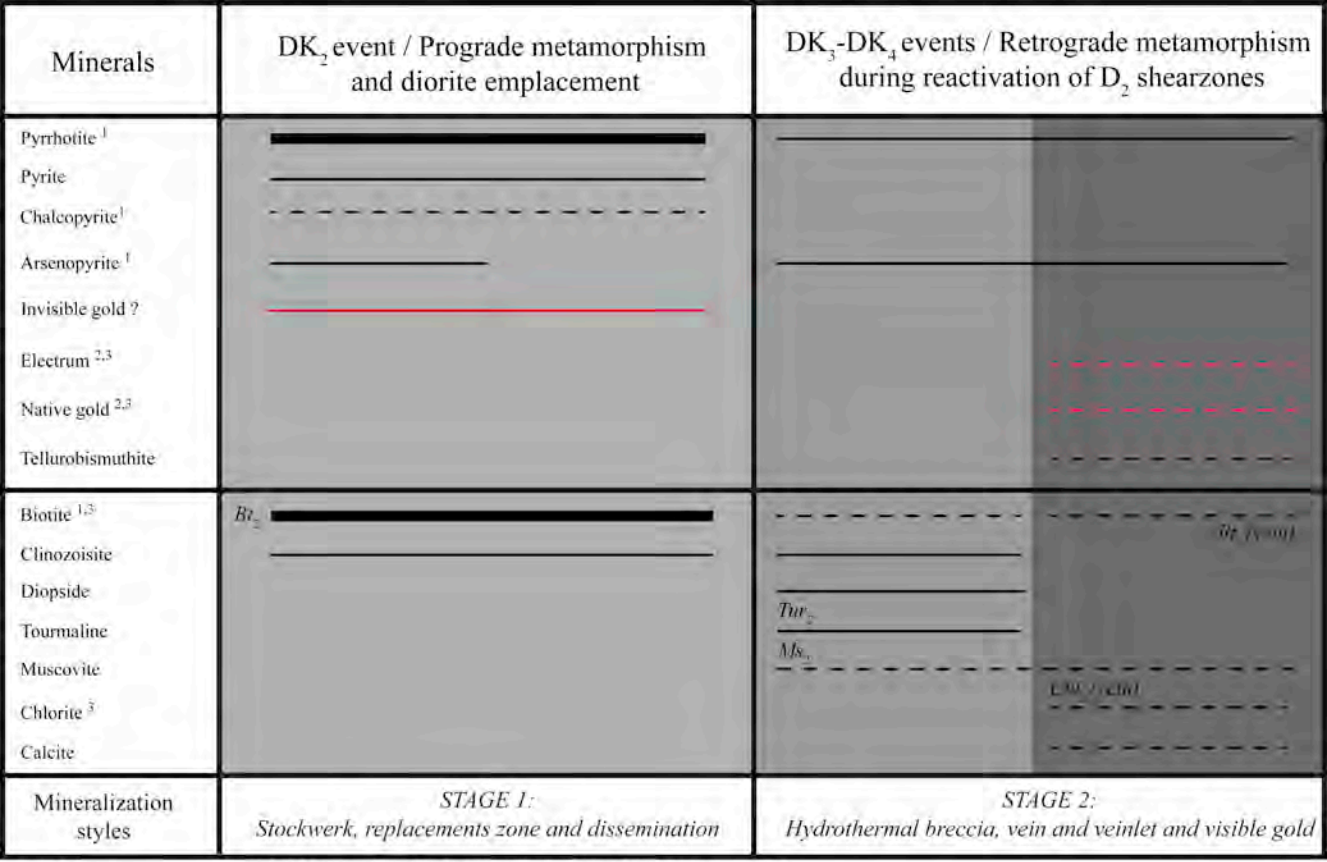
Protolith type	Minerals	Protolith	DK_1 event / Prograde metamorphism	DK_2 event / Prograde metamorphism and diorite emplacement	DK_3-DK_4 events / Retrograde metamorphism during reactivation of D_2 shearzones
			- SK_{2-1} foliation *- PK_1 open folds*	*- SK_2 metamorphic foliation* *- LK_2 mineral lineation* *- PK_2 isoclinal folds* *- DK_2 shear zones*	*- Sinistral displacement and retrogression within D_2-related shear zones* *- DK_3: Hydrothermal breccia* *- DK_4: Chlorite-carbonate veinlets*
Metasediments	Muscovite Quartz Biotite Kyanite Sillimanite Tourmaline Feldspars	*Ms_1* *Tur_1*	*Bt_1*	*Lower amphibolite facies* *Bt_2*	*Ms_2* *Upper greenschist facies* *Bt_3 (vein)* *Tur_2*
Metabasites	Biotite Tourmaline Feldspars Quartz Orthopyroxene Amphiboles Chlorite Calcite Garnet Ilmenite	*Bt_1* *Chl_1*			*Bt_2* *Chl_2 (vein)*
Diorite	Mg-Hornblende Quartz Feldspars Biotite Actinolite Calcite Muscovite				

Major — Minor - - - Rare


A
ALKALINE
nepheline syenite
syenite
syenite
alkali granite
syeno-diorite
granite
ijolite
gabbro
quartz diorite
diorite
SUBALKALINE
gabbro
gabbro
Naba et al. (2004)
Fontaine et al. (this study)
Vegas et al. (2008)
McFarlane et al. (2011)
Na2O + K2O / wt.%
SiO2 / wt.%
B
McFarlane et al. (2011)
Vegas et al. (2008)
Naba et al. (2004)
Fontaine et al. (this study)
Rock/Primitive mantle
Rb Ba Th U Nb Ta La Ce Sr Nd Zr Hf Sm Eu Ti Gd Dy Y Er Yb Lu
C
McFarlane et al. (2011)
Vegas et al. (2008)
Naba et al. (2004)
Fontaine et al. (this study)
Rock/Chondrite
La Ce Nd Sm Eu Gd Dy Er Yb Lu

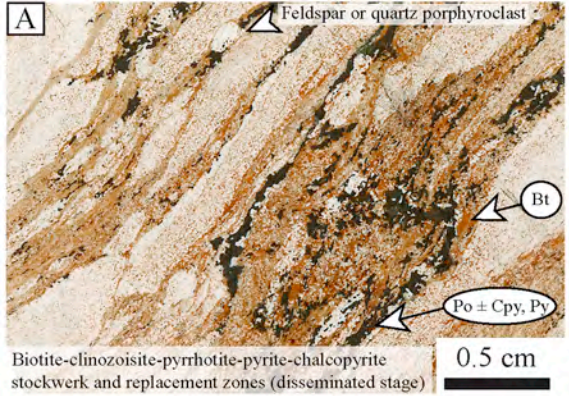

A
SW
NE
axis N94 / 60°
FK1 fold
15 cm
B
NE
SW
LK2 mineral lineation
N0 / 80°
50 cm
C
Mafic rock
Aluminosilicate-bearing metapelites
2 cm
D
SW
NE
(N225 / 79°
Metapelite
Sinistral DK2 shear band
SK2 foliation
Deformation
20 cm
E
Sheath fold?
FK1/FK2 fold interference pattern ?
1 cm
F
231 / 63°
5 cm
(section view)
Aluminosilicate-rich layer in metapelites
Aluminosilicate-poor layer in metapelites
G
FK2 fold with SK2 axial planar cleavage
2 cm


(Equal angle
Lower hemisphere)
SK2 metamorphic foliation (N=14)
LK2 mineral lineation (N=7)
DK3-4 hydrothermal veins (N=61)
FK1 fold axis (N=6)

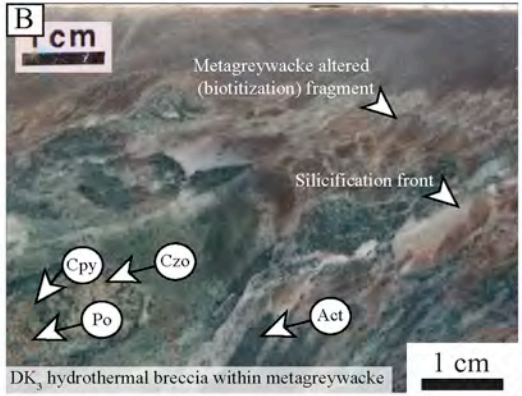


Major
Minor
Rare

1 mainly in alumino-silicate-bearing metapelites and quartz-biotite metagreywacke
2 mainly in quartz-muscovite schist
3 mainly in metabasic rock



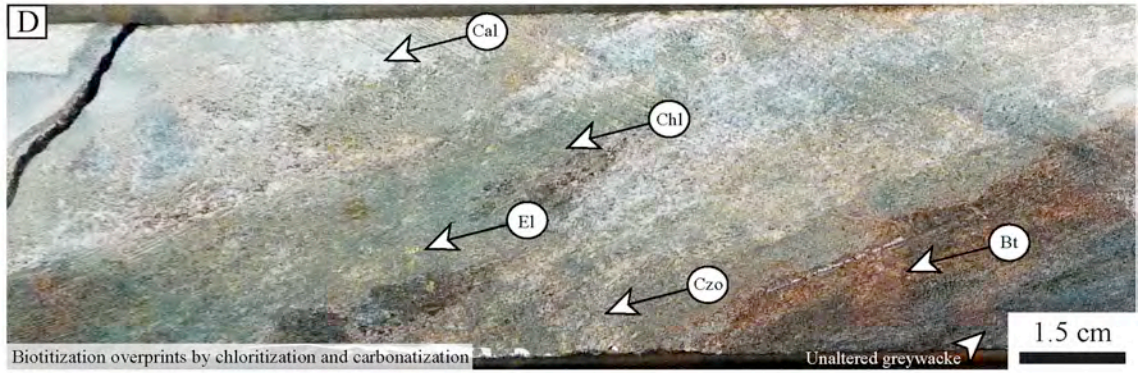
Biotite-clinozoisite-pyrrhotite-pyrite-chalcopyrite stockwerk and replacement zones (disseminated stage)



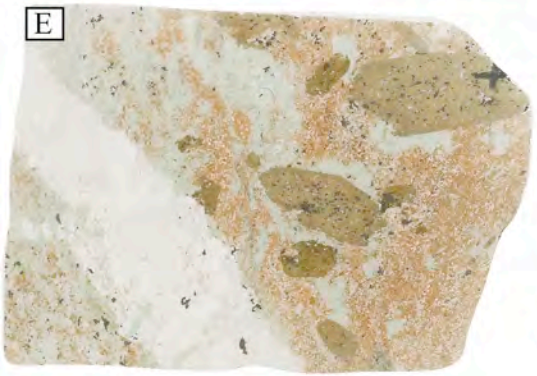
DK_3 hydrothermal breccia within metagreywacke

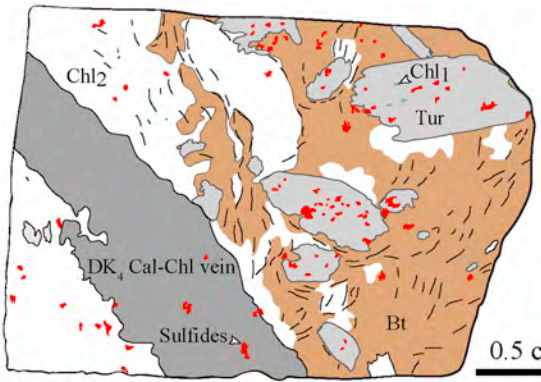


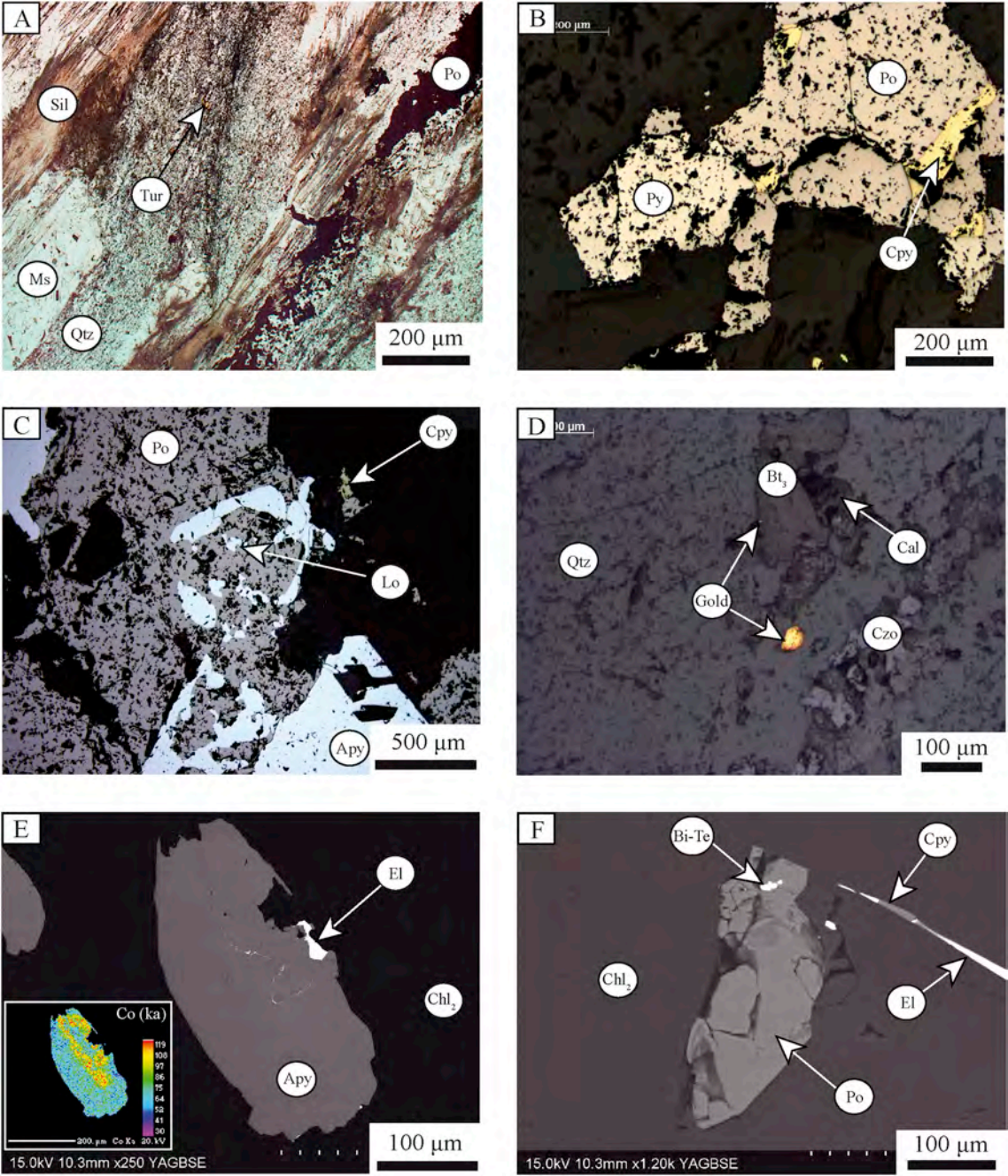
DK_3 diopside-actinolite veins cut by DK_4 carbonate veinlets (vein stage)

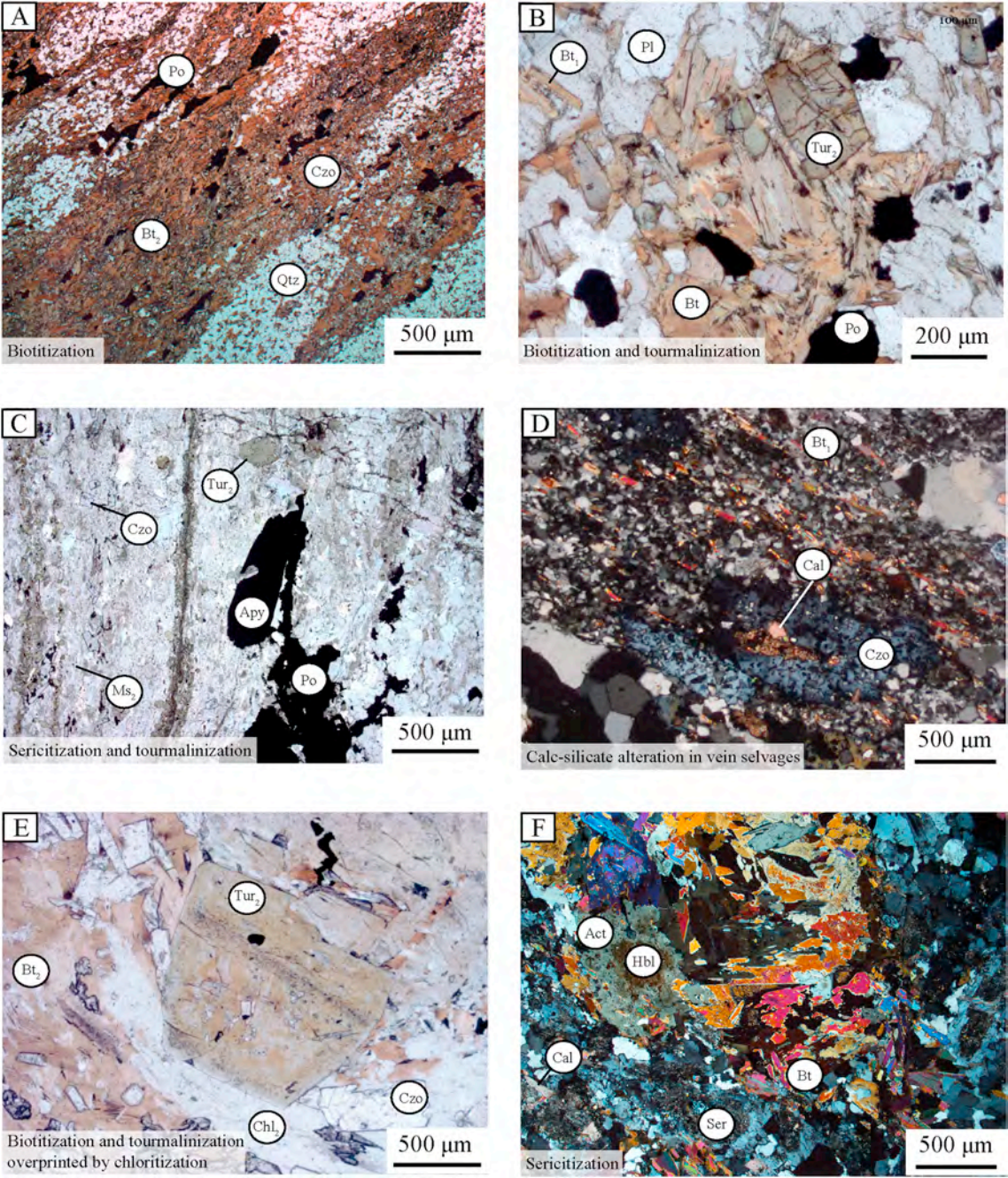


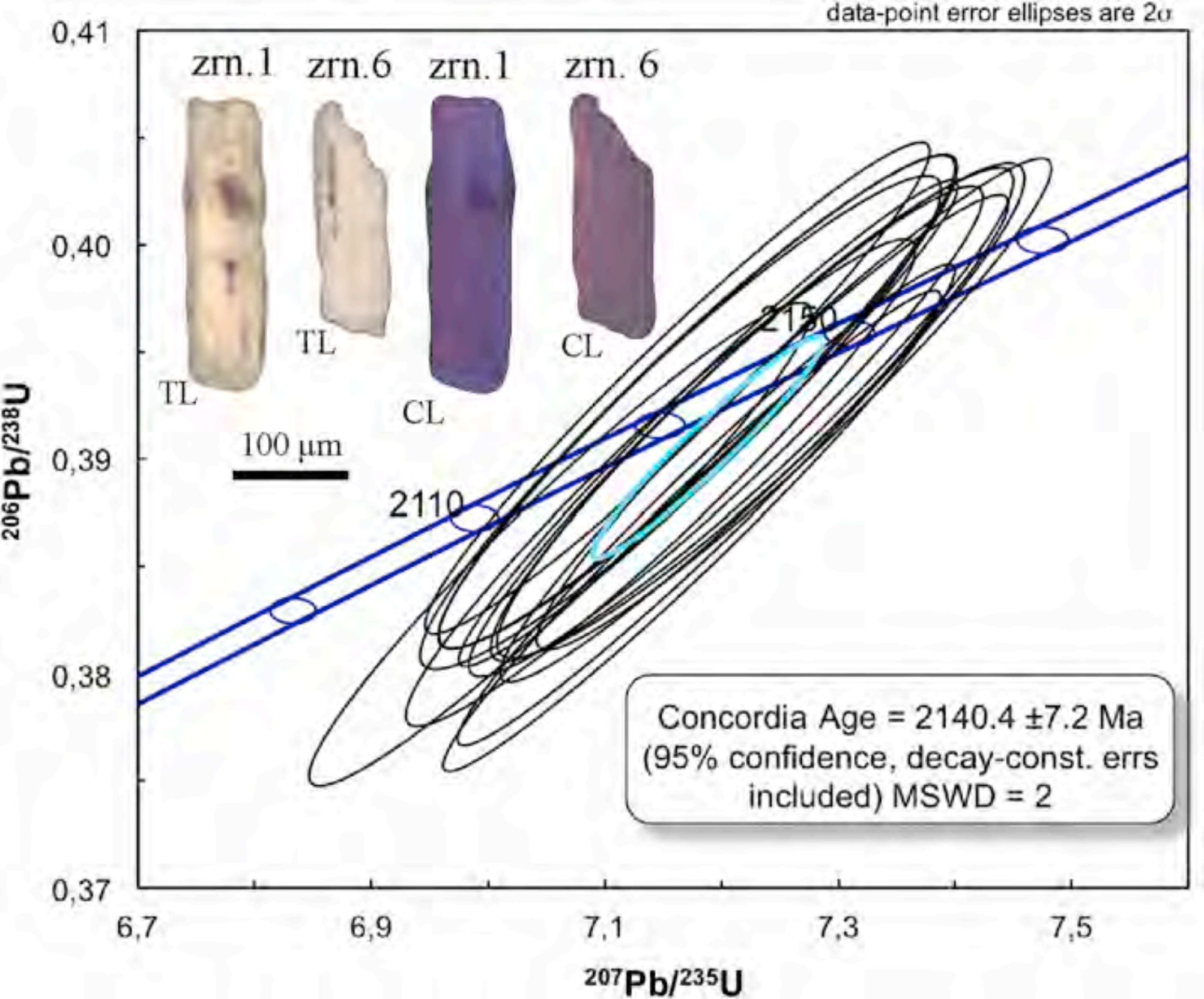
Biotitization overprints by chloritization and carbonatization

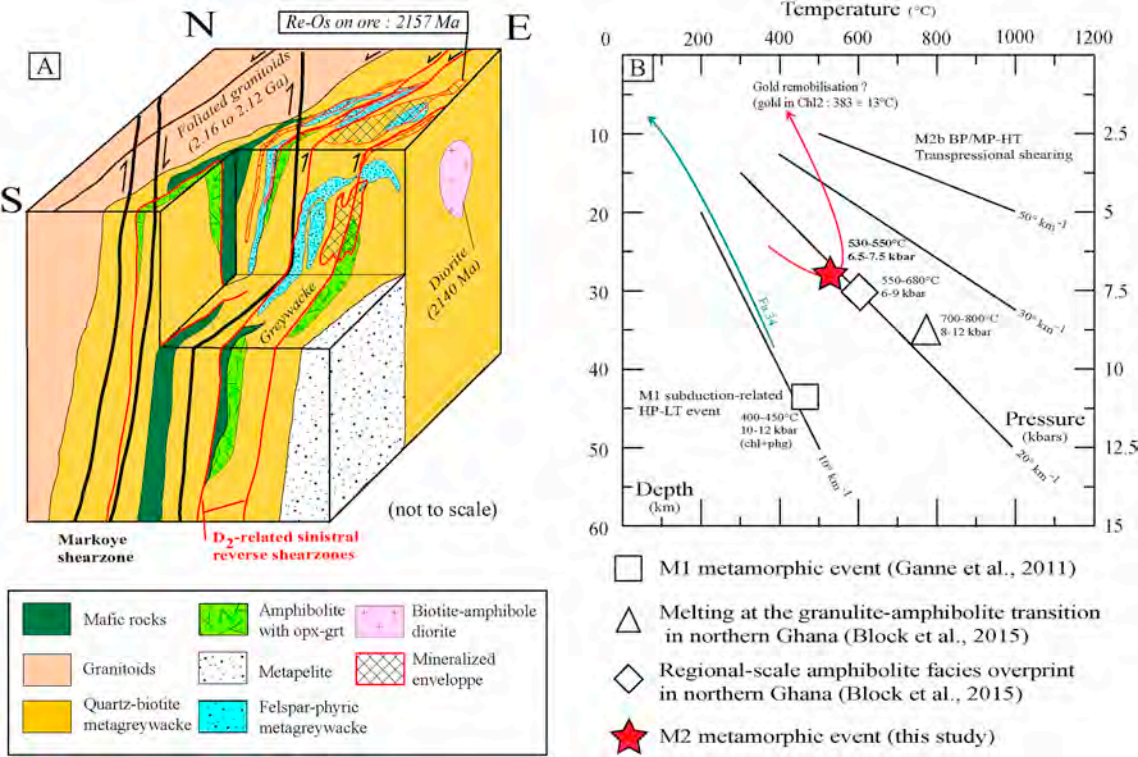


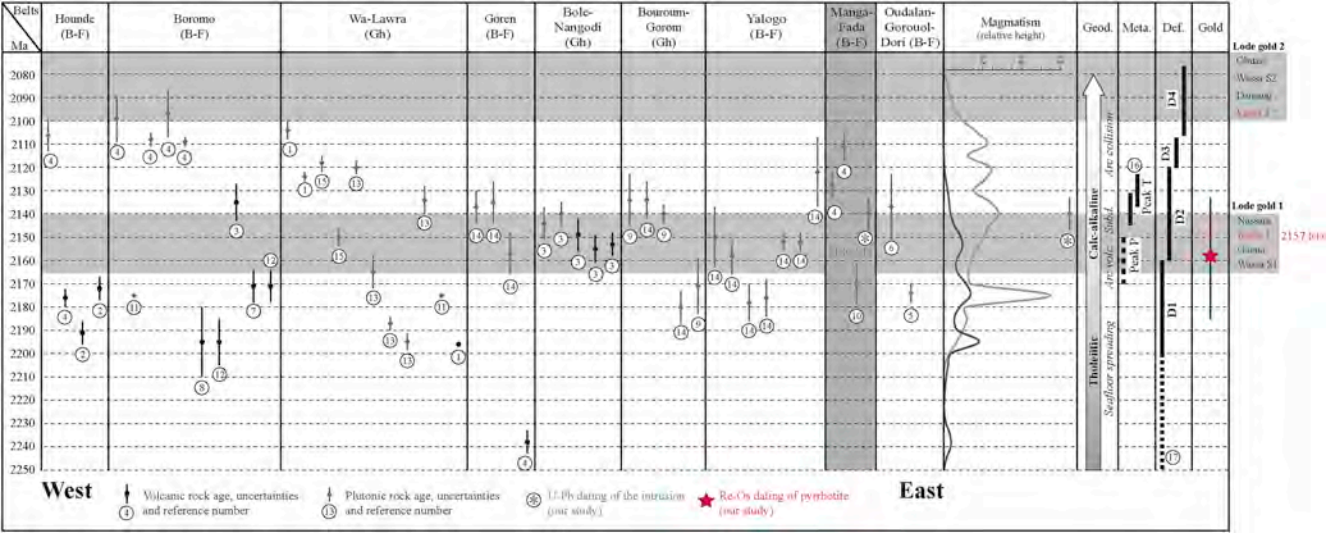



A
Sil
Po
Tur
Ms
Qtz
200 µm
B
Po
Py
Cpy
200 µm
C
Po
Cpy
Lo
Apy
500 µm
D
Bt3
Cal
Qtz
Gold
Czo
100 µm
E
El
Chl2
Apy
Co (ka)
100 µm
15.0kV 10.3mm x250 YAGBSE
F
Bi-Te
Cpy
Chl2
El
Po
100 µm
15.0kV 10.3mm x1.20k YAGBSE


A
Po
Czo
Bt2
Qtz
500 µm
Biotitization
B
Bt1
Pl
Tur2
Bt
Po
200 µm
Biotitization and tourmalinization
C
Tur2
Czo
Apy
Po
Ms2
500 µm
Sericitization and tourmalinization
D
Bt1
Cal
Czo
500 µm
Calc-silicate alteration in vein selvages
E
Tur2
Bt2
Czo
Chl2
500 µm
Biotitization and tourmalinization overprinted by chloritization
F
Act
Hbl
Cal
Bt
Ser
500 µm
Sericitization


data-point error ellipses are 2σ
zrn.1
zrn.6
zrn.1
zrn. 6
TL
TL
CL
CL
100 µm
2110
2150
Concordia Age = 2140.4 ±7.2 Ma
(95% confidence, decay-const. errs
included) MSWD = 2
0,41
0,40
0,39
0,38
0,37
6,7
6,9
7,1
7,3
7,5
206Pb/238U
207Pb/235U


A
N
E
S
Re-Os on ore : 2157 Ma
Foliated granitoids (2.16 to 2.12 Ga)
Greywacke
Diorite (2140 Ma)
(not to scale)
Markoye shearzone
D2-related sinistral reverse shearzones
Mafic rocks
Granitoids
Quartz-biotite metagreywacke
Amphibolite with opx-grt
Metapelite
Felspar-phyric metagreywacke
Biotite-amphibole diorite
Mineralized enveloppe
B
Temperature (°C)
0
200
400
600
800
1000
1200
Gold remobilisation ?
(gold in Chl2 : 383 ± 13°C)
M2b BP/MP-HT
Transpressional shearing
50° km-1
30° km-1
20° km-1
10° km-1
Fe-34
530-550°C
6.5-7.5 kbar
550-680°C
6-9 kbar
700-800°C
8-12 kbar
M1 subduction-related
HP-LT event
400-450°C
10-12 kbar
(chl+phg)
Pressure
(kbars)
Depth
(km)
10
20
30
40
50
60
2.5
5
7.5
10
12.5
15
M1 metamorphic event (Ganne et al., 2011)
Melting at the granulite-amphibolite transition in northern Ghana (Block et al., 2015)
Regional-scale amphibolite facies overprint in northern Ghana (Block et al., 2015)
M2 metamorphic event (this study)


Belts
Ma
Hounde (B-F)
Boromo (B-F)
Wa-Lawra (Gh)
Goren (B-F)
Bole-Nangodi (Gh)
Bouroum-Gorom (Gh)
Yalogo (B-F)
Manga-Pada (B-F)
Oudalan-Gorouol-Dori (B-F)
Magmatism (relative height)
Geod.
Meta.
Def.
Gold
2080
2090
2100
2110
2120
2130
2140
2150
2160
2170
2180
2190
2200
2210
2220
2230
2240
2250
Lode gold 2
Ghana
Wassa S2
Damang
Ayanfuri
Lode gold 1
Nassara
Bonte 1
2157 ±10
Ghana
Wassa S1
Calc-alkaline
Tholeiitic
Arc collision
Slab-d
Arc-relic
Seafloor spreading
Peak T
Peak P
D4
D3
D2
D1
West
East
Volcanic rock age, uncertainties and reference number
Plutonic rock age, uncertainties and reference number
U-Pb dating of the intrusion (our study)
Re-Os dating of pyrrhotite (our study)

ACCEPTED MANUSCRIPT

Geology of the world-class Kiaka gold deposit, West African Craton, Burkina Faso

Hightlights

- A geological framework for the Kiaka gold deposit is proposed for the first time.
- A U-Pb dating on ziron from a diorite intrusion gave a magmatic age of 2140 ± 7 Ma.
- Two stages of hydrothermal alteration and mineralization are recognized.
- D_2-related shear zones control high-grade gold mineralization.
- A Re-Os dating on pyrrhotite (early-stage) gave an age of 2157 ± 24 Ma.

ACCEPTED MANUSCRIPT